JOURNAL OF PETROLOGY | VOLUME 53 | NUMBER 9 | PAGES 1807–1835 | 2012 | doi:10.1093/petrology/egs034

Combining Quantitative Textural and Geochemical Studies to Understand the Solidification Processes of a Granite Porphyry: Shanggusi, East Qinling, China

ZONG-FENG YANG*

STATE KEY LABORATORY OF GEOLOGICAL PROCESSES AND MINERAL RESOURCES, CHINA UNIVERSITY OF GEOSCIENCES, BEIJING, 100083, CHINA

RECEIVED APRIL 1, 2011; ACCEPTED MAY 2, 2012
ADVANCE ACCESS PUBLICATION JUNE 22, 2012

Igneous rock textures reflect the cooling history of the parental magma. Combined with chemical data, they can provide physical and chemical information about the evolution of a magma body. The petrographic textures and chemical compositions of 21 coarse- and fine-grained granite samples along an ~250 m horizontal outcrop of the Shanggusi granite porphyry are presented in this case study. The coarse-grained granite porphyry is an early intrusion, and the fine-grained granite dykes, mostly intruded into the granite porphyry, are later intrusions. The studied samples have nearly homogeneous major element bulk-rock and mineral compositions, but show large variations in their trace element compositions and textural characteristics. The trace element data suggest the influence of hydrous fluids (possibly enriched in CO_2, F, and Cl) in the evolution of the plutonic body. Textural analysis of the coarse-grained granite porphyry indicates that the crystal size distribution (CSD) slopes, intercepts and total numbers of groundmass decrease from the center to the margin of the intrusion in contrast to the maximum diameter of the crystals (L_{max}) (average length of the four largest quartz crystals for each sample); however, most fine-grained samples and the groundmass of the coarse-grained samples show concave-down CSDs, indicating textural coarsening. Quartz CSDs in the coarse-grained samples are kinked, with a steep-sloped log–linear section representing small crystals (<1 mm) and a shallow-sloped log–linear section representing large crystals (>1 mm). These two crystal populations are interpreted as resulting from a shift in cooling regime. The straight CSDs of two fine-grained samples may be due to a different cooling history. In general, the spatial variation of the CSD patterns can be attributed to various degrees of overgrowth and mechanical compaction. The quartz phenocrysts in several coarse-grained samples exhibit a high degree of alignment, which may be the result of magmatic flow. By integrating the field geology, geochemistry and quantitative textural data from the horizontal profile of the Shanggusi granite porphyry, it is suggested that hydrous fluids at the top of the intrusion not only controlled the fractionation of elements but also affected its cooling history. Fluid migration-controlled undercooling can explain the solidification processes in the Shanggusi intrusion, and may also be prevalent in other fluid-rich shallow intrusions. Quantitative integration of textural and geochemical data for igneous rocks can contribute to our understanding of the relationships between physical and chemical processes in a magma system, and provide relatively comprehensive insights into the petrogenesis of granites.

KEY WORDS: *Shanggusi; granite porphyry; solidification processes; crystal size distributions; fluids; undercooling*

INTRODUCTION

A fundamental issue in igneous petrology is to understand the magma solidification process, and in particular to clarify which physical and chemical processes control the characteristics of the final product. Typically, a variety of complex magma solidification processes can be investigated by studying suites of comagmatic rocks that have different chemical and textural characteristics. However, it is

*Corresponding author. E-mail: yangzfeng2008@163.com

difficult to examine and verify the physical processes of magma solidification in terms of traditional geochemical and qualitative petrographic studies, especially for crystal nucleation and growth, which, to a large extent, are independent of the chemical composition of the system. Depending on their cooling history, magmas with the same composition can solidify into rocks with dramatically different physical appearances. For example, equigranular granite, granite porphyry and rhyolite show three different solidification processes in their textural characteristics, whilst having similar chemical compositions. Thus, if we wish to understand the textural differences within a single compositional type of rock in order to constrain the cooling history and solidification processes, the textures of the rocks need to be quantified.

In recent years, following the work of Marsh (1988), who first introduced the theory of crystal size distributions (CSDs) for magmatic systems, quantitative textural analysis of igneous rocks combined with their geochemical study has been increasingly applied to investigate magmatic processes (e.g. Cashman & Marsh, 1988; Mock *et al.*, 2003; Boorman *et al.*, 2004; Higgins, 2006*a*; Higgins & Roberge, 2007; Morgan *et al.*, 2007; O'Driscoll *et al.*, 2007; Salisbury *et al.*, 2008; Higgins & Meilleur, 2009; Pappalardo & Mastrolorenzo, 2010; Vinet & Higgins, 2010). Some magmatic processes, such as magma flow (e.g. Higgins, 2002*a*), compaction and compaction-driven recrystallization (e.g. Boorman *et al.*, 2004; Williams *et al.*, 2006), and textural coarsening (e.g. Higgins, 1998, 1999, 2009; Higgins & Roberge, 2003; Magee *et al.*, 2010) are better examined by quantitative textural studies rather than geochemical studies. In particular, textural coarsening of igneous rocks, which may be as important a process as fractional crystallization, does not change the chemical composition of the rocks and can be investigated only by quantitative textural analysis (Higgins, 2011, and references therein).

The solidification of magma is a result of a complex interplay between crystallization and dissolution (e.g. Higgins & Roberge, 2003; Armienti *et al.*, 2007). Crystal nucleation, growth and dissolution are strongly dependent on the degree of undercooling, which in turn is controlled by both the actual crystallization temperature and the liquidus temperature. The undercooling of magma in a chamber can be modified by addition of hotter magma, or by the reduction of total or partial pressure during ascent of the magma. When a pulse of magma begins to crystallize, and the liquidus temperature of the residual melt is reduced only within a very limited range as the result of crystallization that continually changes the crystallizing melt composition, the undercooling in different locations in the magma chamber is mainly controlled by the actual crystallization temperature, which has a close relationship with the isotherms. Such cooling histories have been theoretically modeled and verified by the spatial textural variation of natural samples (e.g. Zieg & Marsh, 2002; Nkono *et al.*, 2006; Patwardhan & Marsh, 2011). However, the liquidus temperature of the melt typically can be significantly changed by variations in fluid content or fluid circulation in the magma or residual magma, giving rise to variations in the degree of undercooling. If the change in the undercooling of a magma chamber mainly results from the variation of the liquidus temperature rather than that of the actual temperature (e.g. Higgins, 2002*a*), the textural variations within the plutonic body would not be consistent with those predicted from the isotherms. In addition, the migration and accumulation of fluids may result in chemical fractionation within the magma body. Hence, combining quantitative textural and geochemical studies may help us to investigate such processes.

In this study, observations were made of the field geology, mineralogy and petrology, and were combined with quantitative textural and geochemical analysis of the Shanggusi granite porphyry. The results show that the spatial variations in the CSD parameters are not consistent with those controlled by isotherms: the center of the intrusion has a much higher undercooling than its margins. It is argued that this phenomenon is closely related to the migration and heterogeneous accumulation of fluids at the top of the intrusion, which might also play an important role in chemical variation within the intrusion.

GEOLOGICAL SETTING AND SAMPLE DESCRIPTIONS

Geology of the Qinling–Dabie orogen

The Qinling–Dabie orogen extends more than 1500 km across central China (Fig. 1a). The western segment is called the Qinling region and the eastern segment is called the Dabie region. The Qinling–Dabie orogen comprises two sutures and three blocks (Meng & Zhang, 1999, 2000). The Shangdan suture separates the North China Block (including the North Qinling belt) from the Qinling microplate (the South Qinling belt), and the Mianlue suture separates the Qinling microplate from the South China Block. The Shangdan suture is generally considered to have formed following subduction of the Shangdan ocean and multi-stage accretion of the South Qinling belt to the North Qinling belt. The suture represents a Middle Palaeozoic subduction–collision event followed by Mesozoic–Cenozoic intraplate strike-slip faulting (Mattauer *et al.*, 1985; Zhang *et al.*, 1989; Ratschbacher *et al.*, 2003; Wang *et al.*, 2005). The Mianlue suture was formed by the Triassic collision between the South Qinling belt and the South China Block (Zhang *et al.*, 2004). The North Qinling belt, bounded by the Machaoyin fault zone and the Shangdan suture (Fig. 1a), is composed predominantly of Proterozoic to Palaeozoic

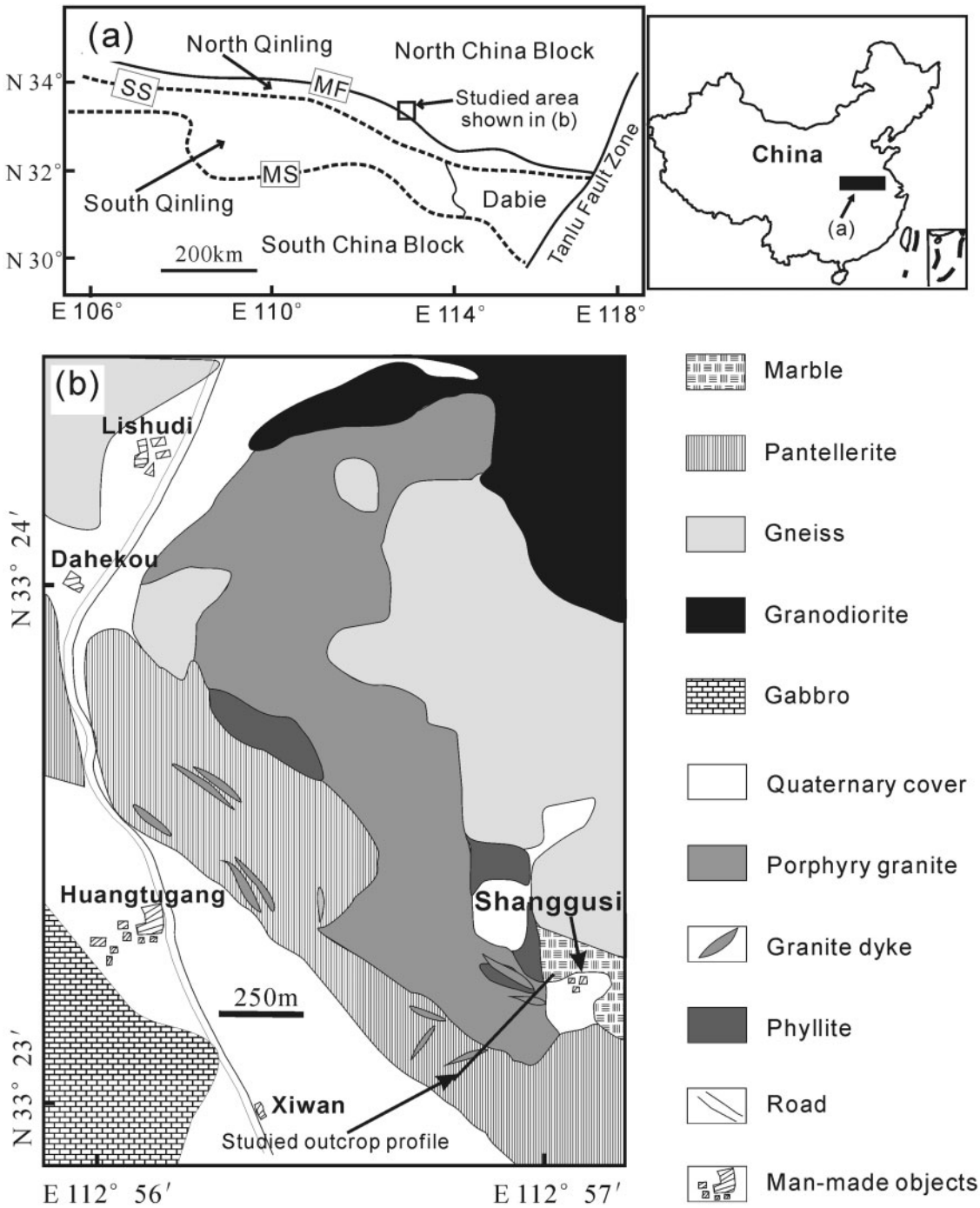

Fig. 1. (a) General geological map of the Qinling–Dabie orogen showing its regional tectonic setting (after Meng & Zhang, 2000) and the location of the Shanggusi intrusion (outlined by black square); MF, Machaoyin fault; MS, Mianlue suture; SS, Shangdan suture. (b) Geological map of the Shanggusi area showing the major lithological units and the location of the studied granite porphyry (after Yang *et al.*, 2011).

medium-grade metasedimentary and metavolcanic rocks. The Qinling complex constitutes the Precambrian basement of the Qinling–Dabie orogen (Hu *et al.*, 1993; You *et al.*, 1993; Wang *et al.*, 2003). The South Qinling belt is bounded to the north by the Shangdan suture and to the south by the Mianlue suture (Fig.1), and comprises a thick pile of Late Proterozoic to Triassic sediments overlying an Early Proterozoic crystalline basement. Three pulses of

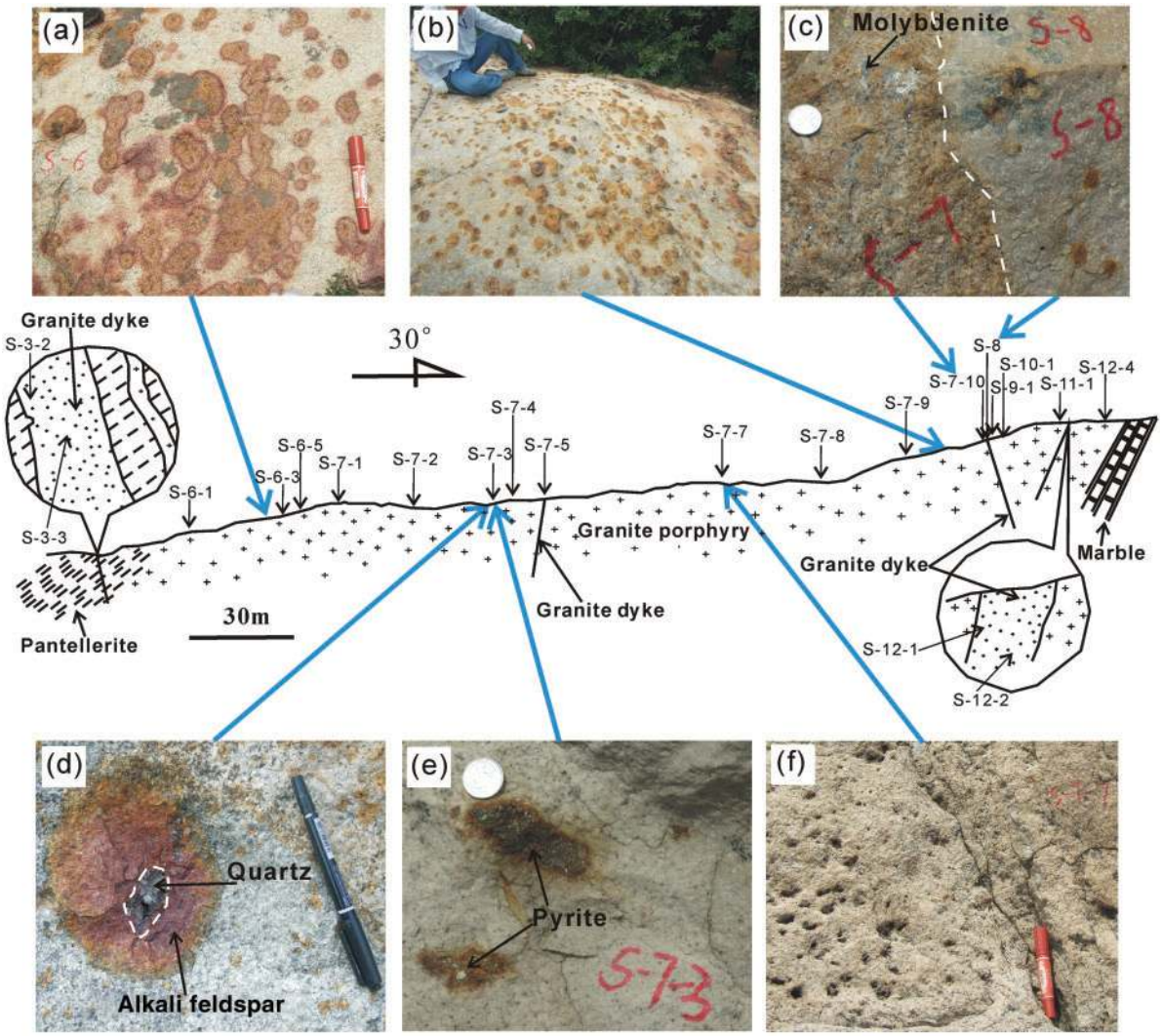

Fig. 2. Field photographs and sample locations across the Shanggusi outcrop profile. (a, b) Miarolitic cavities that contain altered pyrite; these occur in both sides of the profile. (c) A representative granite dyke (right) intruded into the granite porphyry; the contact is curved and indistinct (note the disseminated molybdenite in the coarse-grained granite porphyry). (d) A large miarolitic cavity showing reddish-brown alkali feldspar surrounding quartz. (e) Representative photograph of unaltered pyrite in the coarse-grained granite porphyry. (f) Miarolitic cavities, without significant amount of pyrite, at the center of the profile. The pens shown for scale are ~14 cm in length. The coin for scale is ~2·4 cm in diameter.

granitoid magmatism and Mo mineralization have been recognized, corresponding to significant tectonic events in the East Qinling–Dabie oregen (e.g. Mao *et al.*, 2008).

Geology of the Shanggusi granite porphyry and sampling

The Shanggusi granite porphyry, situated in the southern margin of the North China Block, is a newly discovered porphyry-type molybdenum deposit in east Qinling (Yang *et al.*, 2011) (Fig. 1a). Re–Os dating of disseminated molybdenite in the Shanggusi granites yields emplacement ages ranging from 122·5 (±2·1) Ma to 124·8 (±1·8) Ma (Yang *et al.*, 2010). Figure 1b shows the fundamental geological characteristics of the Shanggusi granite porphyry. It covers an area of *c.* 1·5 km^2 bounded by the granodiorite to the north, pantellerite to the SW and gneiss to the east. A number of granite dykes occur within or surround the granite porphyry body; most of them are emplaced into the pantellerite (Fig. 1b). A profile *c.* 250 m long in the southern part of the granite porphyry outcrop was investigated and sampled in the field (Fig. 2).

Evidence for magmatic fluid phase exsolution is provided by miarolitic cavities (e.g. Candela, 1997) within the outcrop (Fig. 2a–f). These cavities consist mainly of quartz and alkali feldspar (Fig. 2d), and commonly also contain pyrite, which is usually altered to brown limonite at both

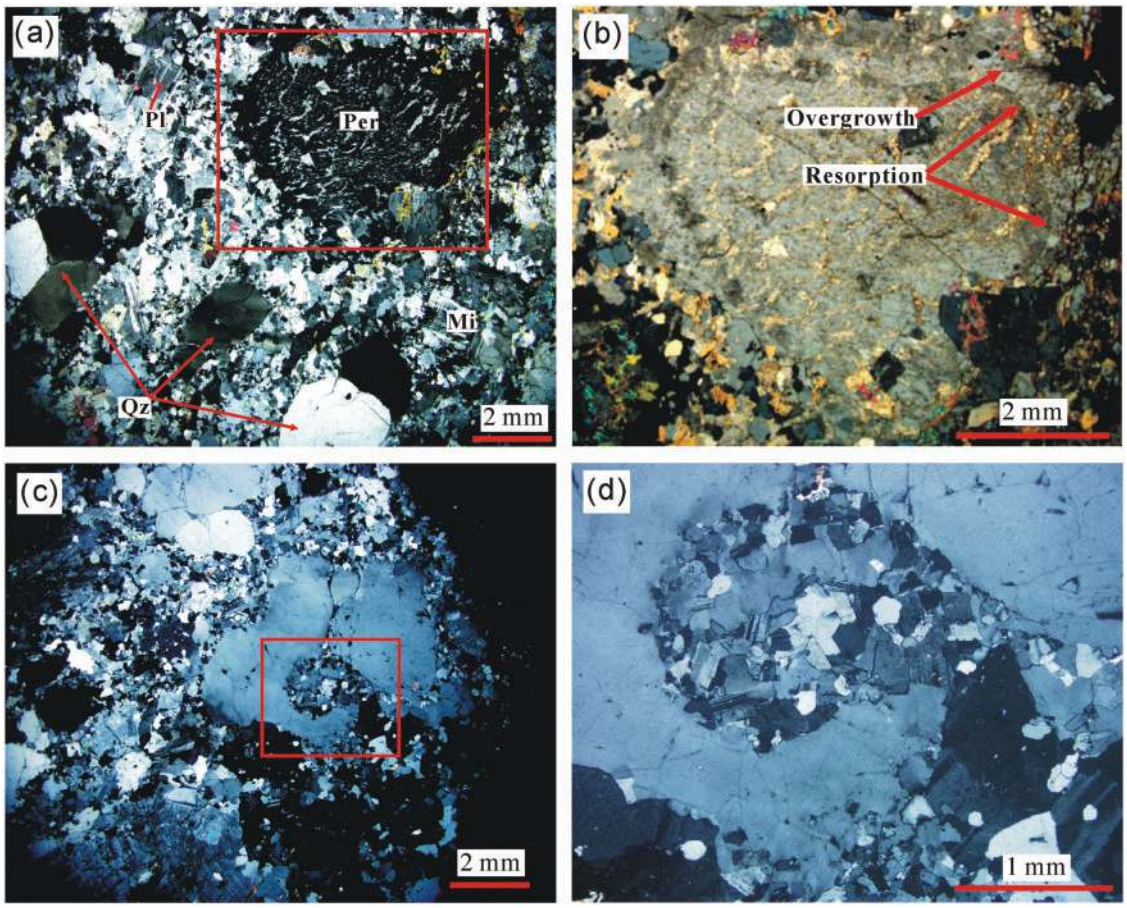

Fig. 3. Representative photomicrographs showing the textural characteristics of the granite porphyry. (a) Typical phenocrysts of quartz and alkali feldspar (perthite). Quartz phenocrysts are rounded and show embayments because of resorption. (b) Magnified view of (a) with insertion of a wave plate with a retardation of 137 nm. The perthite shows an overgrowth rim and does not show embayments like the quartz phenocrysts. (c) Typical rounded embayment in a quartz phenocryst. The magnified view in (d) clearly shows the eutectic crystallization of fine-grained quartz and feldspar in the resorbed region of the quartz phenocryst. Mi, microlite; Per, perthite; Pl, plagioclase; Qz, quartz.

ends of the profile (Fig. 2a–e). In contrast, pyrite or other ore minerals are rare in the center of the profile, and only a few miarolitic cavities were observed there (Fig. 2f).

Twenty-one samples were collected from the profile. These were preliminarily divided into two categories based on their qualitative petrographic characteristics in the field. The sample set includes 13 coarse-grained samples that contain quartz and feldspar phenocrysts and eight fine-grained samples without phenocrysts. Among these samples are six fine-grained samples collected from granite dykes that are emplaced into the granite porphyry or the adjacent pantellerite. The exact locations of each sample and typical field petrographic characteristics are indicated in Fig. 2.

The major rock-forming minerals in all the samples are quartz (20–40%), alkali feldspar (25–40%) and Na-plagioclase (30–50%). Figure 3 shows representative petrographic characteristics of the coarse-grained samples. The striking porphyritic texture typically shows resorption of quartz and alkali feldspar phenocrysts. The rounded, embayed morphology of quartz can be clearly seen under crossed polars (Fig. 3a, c and d); resorption of perthitic alkali feldspar, surrounded by subsequent overgrowth rims, is more easily seen when a wave plate with a retardation of 137 nm is inserted into the polarizing microscope (Fig. 3b). The petrographic characteristics of the fine-grained samples are discussed in more detail below.

ANALYTICAL METHODS

Crystal size distributions

CSD theory

If the number of crystals (per unit size range) in an igneous rock is plotted against their relative size, in a semi-logarithmic fashion, many rocks show remarkably smooth, often linear trends with negative slopes. This relationship can be explained by CSD theory, which allows crystal size data to be used as a method of determining

some of the crystallization kinetics of magmatic systems independent of experimental approaches or thermodynamic or kinetic models (e.g. Cashman & Marsh, 1988; Resmini & Marsh, 1995; Marsh, 1998, 2007; Higgins, 2002*a*, 2011; Higgins & Roberge, 2003; Boorman *et al.*, 2004; Higgins & Chandrasekharam, 2007; Resmini, 2007; Moss *et al.*, 2010). CSD theory is based on a parameter called population density, which is used to develop the general crystal population balance equation. To establish the crystal population balance in a magma body, the number of crystals of a given size, per unit volume of magma, the population density (n), must be known as a function of crystal size (L). A plot of $\ln(n)$ vs L for a steady-state system, which is continuously fed and emptied, will be a line with a slope of $-1/Gt$ and intercept n^0, where G represents the growth rate, t is the residence (or growth) time and n^0 is the final nucleation density (when crystal size approximates to zero) (Marsh, 1988, 1998). If either the residence time or the growth rate is known, the other may be determined. Although the above formulation was developed for steady-state systems, it can be shown that for a non-steady-state, batch-cooling, model, in which the magma is not allowed input or output of crystals, and under certain conditions (e.g. exponentially increasing nucleation rate with a constant growth rate), the relation has the same form as the steady-state model (Marsh, 1988, 1998). The most important assumption of the two end-member CSD models is constant crystal growth rate (G). Kinking or curvature in CSD plots has been attributed to processes such as crystal accumulation and removal (e.g. Marsh, 1988, 1998), compaction (e.g. Boorman *et al.*, 2004), mixing of crystal populations (e.g. Higgins, 1996; Turner *et al.*, 2003; Vinet & Higgins, 2010) and post-nucleation crystal ageing caused by annealing or Ostwald ripening (e.g. Higgins, 1998, 1999, 2002*a*, 2011; Higgins & Roberge, 2003).

Method

All the samples contain three major crystal populations of quartz, alkali feldspar, and Na-plagioclase. Among these, quartz was chosen for quantitative textural analysis as it is the most abundant phenocryst phase in the granite porphyry. Furthermore, it is the most resistant one to post-alteration and therefore may preserve its original grain morphology. The other minerals are not sufficiently fresh in thin section for accurate textural analysis. Regular thin sections were used for textural analysis and the methods used generally follow those presented by Higgins & Roberge (2003). We first prepared digitized images, examples of which are shown in Figs 4 and 5. To identify and outline the quartz crystals more accurately, a wave plate with a retardation of 137 nm was inserted into the polarizing microscope (Fig. 4c). For touching crystals that are at extinction or have the same interference color in the digitized images, the quartz crystals were identified by rotating the microscope stage as shown in Fig. 6. This procedure was carried out only to increase the accuracy of analysis. More than 300 crystals were analyzed in each sample. The greyscale image was analyzed using the program *ImageJ*, a Java version of the popular program *NIHImage*. The raw positional data were reduced to intersection parameters using a specially written program. The CSD of crystals was calculated with the program *CSDCorrections 1.38* (Higgins, 2000).

The mean crystal shape is expressed by the crystal aspect ratio *S*:*I*:*L* (short:intermediate:long dimensions). The shape aspect ratio Short/Intermediate is estimated from the mode of the distribution of intersection widths/intersection lengths (Higgins, 1994, 2000). The ratio Intermediate/Long is more complicated to determine; simple modeling of populations of parallelepipeds has been shown to yield imprecise results for some crystal shapes (Garrido *et al.*, 2001; Higgins, 2006*a*). The *CSDSlice* program of Morgan & Jerram (2006) calculates a best fit for the 2D aspect ratios and compares these directly with curves for known crystal shapes. However, the calculated CSD volume using the aspect ratio determined from this method always yields a significantly higher volume than that determined from the total area of the intersections measured, which might result from the complicated crystal shapes of quartz (e.g. Mock & Jerram, 2005). Thus, the ratio Intermediate/Long is estimated by comparison between the quartz volumetric proportion determined from the total area of the intersections measured and the volumetric proportion determined from the CSD (e.g. Higgins, 2002*b*). The crystal shapes of quartz used in this study range from 1:1·54:1·54 to 1:1·96:1·96 based on the average aspect ratio for each sample (Table 1). The crystals were considered to have a roundness of 0·6 or 0·7. Logarithmic length intervals were used such that each bin is $10^{0.125}$, $10^{0.167}$ and $10^{0.2}$ times the size of the previous bin according to the crystal number and the accuracy of each CSD plot. Bins with fewer than five crystals were removed from the CSD as they are not precise. The lower limit of the CSD is the smallest crystal that could be easily measured, typically 0·05 mm, and not the smallest crystals in the rock.

Because the CSDs of the fine-grained samples determined here are only slightly curved on a classical CSD diagram [S-type distribution of Higgins (2006*b*)], meaningful values for the slope and intercept of the CSD could be determined by linear regression using the methods of Higgins (2006*b*). The 'goodness of fit', Q, is a parameter that describes how well the data fit to a straight line, taking into account the error in each point. A value greater than 0·1 indicates a very significant fit, but values greater than 0·01 are acceptable (Higgins, 2006*b*). The strongest curved CSDs will have very small values of Q. It is easier to understand CSD dynamics if the characteristic lengths (CL = −1/slope) are considered rather than the slopes, as

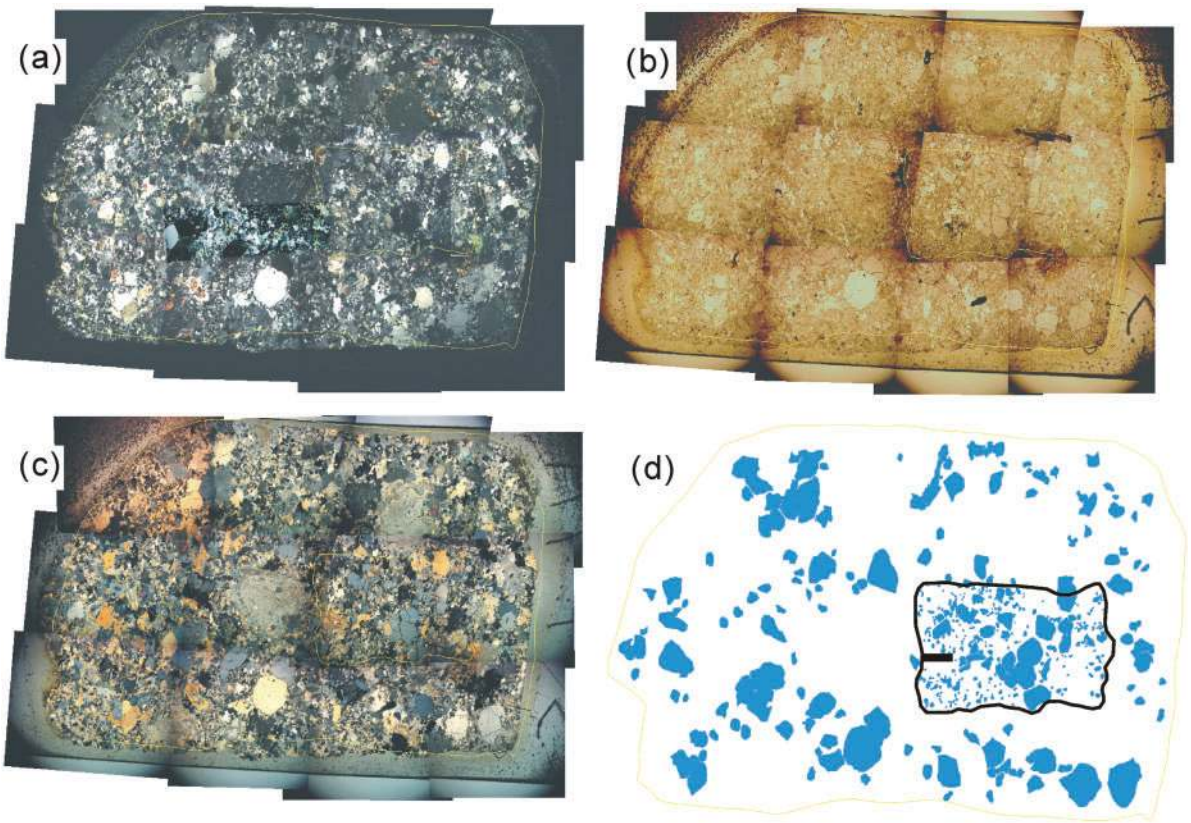

Fig. 4. Representative characteristics of sample S-7-7A in a stitched photomicrograph and digitized image. (a, b, c) Optical photomicrograph under crossed polars, plane polars and crossed polars with wave plate of 137 nm respectively. (d) Digitized outlined image of quartz, where the region outlined in black was used for the textural analysis of the groundmass; the scale bar represents 2 mm. This sample shows a distinct crystal size contrast between the phenocrysts and the groundmass. The phenocrysts mainly consist of quartz (note some of them are resorbed with rounded morphology) and alkali feldspar.

they have the units of length. For crystals that have a perfect semi-logarithmic size distribution, the characteristic length is equal to the mean size.

Spatial distribution patterns

Analysis of the spatial distribution of crystals in rocks is another method of quantifying igneous texture (e.g. Jerram *et al.*, 1996). Such analysis can be used to understand whether crystals are clustered or randomly distributed, and has implications for discerning between differing models of the crystallization of igneous rocks (Jerram *et al.*, 1996, 2003). Furthermore, experimental work has identified characteristic trends for mechanical compaction, sorting and overgrowth on spatial distribution plots (Jerram *et al.*, 1996).

A method for quantifying the spatial distribution pattern (SDP) of grains and crystals in thin section, by calculating an R value, where R is a quantification of the SDP, was introduced by Jerram *et al.* (1996). In a random distribution of points, $R=1{\cdot}0$; $R>1{\cdot}0$ indicates an ordered array of points whereas $R<1{\cdot}0$ indicates a clustered array of points (see Jerram *et al.*, 1996).

Alignment factor

To obtain the degree of alignment of the quartz crystals in the granite porphyry, the AF (alignment factor) is calculated on the 40 largest grains in each sample following Boorman *et al.* (2004) and Williams *et al.* (2006), as the larger grains primarily define the foliation in these rocks. An AF of 100 indicates perfect alignment of the crystals and a value of zero indicates a random arrangement with no alignment (e.g. Boorman *et al.*, 2004; Williams *et al.*, 2006).

Geochemical analysis

Twenty-one representative samples selected for major and trace element analysis were reduced to chips after removal of altered surfaces. The chips were then pulverized into powders using agate mortars. Bulk-rock major and trace element compositions were determined at the Chinese Academy of Geological Sciences. Major elements were determined by X-ray fluorescence (XRF); ferrous iron was determined by a wet chemical method. The accuracies of the XRF analyses are estimated to be 1% for SiO_2, 2% for other major oxides present in concentrations greater than 0·5 wt %, and 5% for minor oxides present in

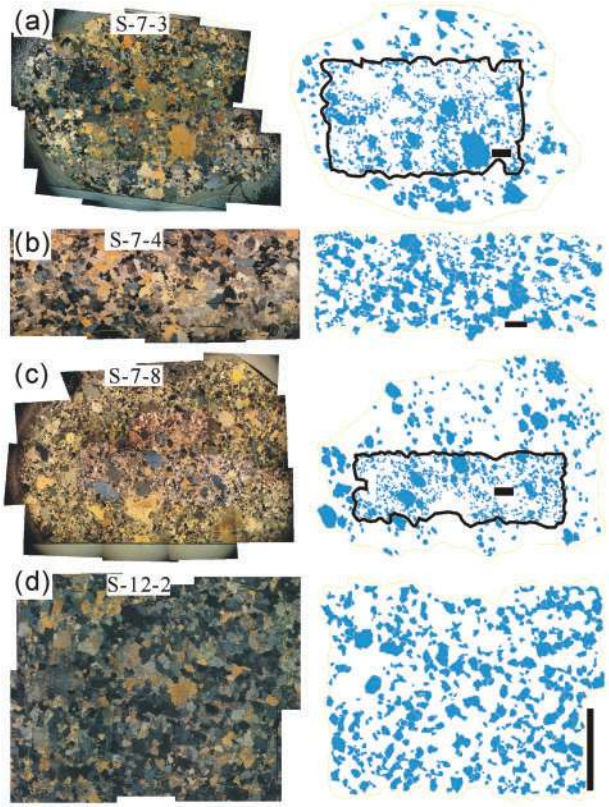

Fig. 5. Representative photomicrographs and outlined quartz images for coarse- and fine-grained samples. (a–c) Samples from the granite porphyry; (d) a sample from a granite dyke. (a) and (c) are coarse-grained samples; (b) and (d) are fine-grained samples; (c) has the most well-developed porphyritic texture; (b) and (d) have an almost equigranular texture; (a) has intermediate textural characteristics between (b) [or (d)] and (c). The regions in (a) and (c) outlined in black were used for textural analysis of the groundmass; scale bars in these outlined images represent 2 mm.

concentrations between 0·01 and 0·5 wt %. Trace element abundances were determined by inductively coupled plasma-mass spectrometry (ICP-MS), following Dulski (1994). The accuracies of the ICP-MS analyses are estimated to be better than 5% (relative) for most elements.

Mineral compositions were determined using a JXA-8100 electron microprobe at the Analytical Laboratory, Beijing Research Institute of Uranium Geology. Analytical conditions involved an acceleration voltage of 20 kV, a beam current of 10 nA, beam diameter of 2–5 μm, and counting times of 10–20 s for peaks and 5 s for background for each element. Measured data were corrected by the ZAF method. Relative analytical uncertainty is <1%.

RESULTS

Mineral chemistry

Electronic Appendix 1—data (available for downloading at http://www.petrology.oxfordjournals.org) presents the microprobe data for the major and accessory rock-forming minerals in the granite porphyry and granite dykes. The plagioclase in all of the samples is albite, ranging from $An_{0·89}Ab_{98·8}$ to $An_{6·29}Ab_{92·7}$ and from $An_{0·2}Ab_{99·4}$ to $An_{3·9}Ab_{95·6}$ for the fine- and coarse-grained samples respectively (Table 1 of Electronic Appendix 1—data). The alkali feldspars are all K-feldspars, with chemical compositions that vary from $Ab_{5·1}Or_{94·9}$ to $Ab_{2·8}Or_{97·2}$ and from $Ab_{6·1}Or_{93·7}$ to $Ab_{1·7}Or_{98·3}$ for the fine- and coarse-grained samples respectively.

The accessory minerals are mainly hematite, pyrite, rutile, zircon, apatite, niobite and bastnasite (Fig. 7). Their chemical compositions are shown in Table 3 of Electronic Appendix 1 and indicate that the accessory minerals may be the main carrier of trace elements. Rare muscovite is an iron-rich ferrimuscovite (Table 2 of Electronic Appendix 1)

CSD data

CSD data for all the samples are presented in Table 1 and CSD plots are illustrated in Fig. 8. The outlined images of quartz crystals and raw data output from the *CSDCorrections 1.38* program for all the samples are provided in Electronic Appendix 1—data and Appendix 2—digitized images.

The CSD curves for all the samples have negative slopes and turn down at the lower size bins on the semilogarithmic CSD diagrams (Fig. 8a–d). If the concave-down parts of the lower size bins are not considered, the CSDs of the fine-grained samples all have $Q > 0·01$ (Table 1), and hence have a very significant fit to a straight line (Fig. 8a). The coarse-grained samples, except sample S-7-3 and S-7-8, have curved to concave-up CSDs ($Q < 0·01$) (Fig. 8b). However, because there were not sufficient large quartz crystals outlined for these two samples, in which many more quartz phenocrysts are present, the two samples are also considered have curved to concave-up CSDs ($Q < 0·01$) (Fig. 8c). When the CSD data for the fine-grained samples and the groundmass of the coarse-grained samples are plotted on cumulative distribution function (CDF) diagrams (Higgins, 2006*b*), they clearly show log-normal CSDs (L-CSD) (Fig. 8e). The curved concave-up CSDs of the coarse-grained samples are similar to fractal CSDs (F-CSD) (Higgins, 2006*b*) if the concave-down parts are not considered (Fig. 8f). However, here two separate straight CSDs for the groundmass and phenocrysts of the coarse-grained samples are observed (Fig. 8c). These straight CSDs typically demonstrate the textural characteristics of the granite porphyry. CSD shapes and ranges are fairly consistent for the coarse- and fine-grained samples, respectively, but with local deviations from the main trend. The notable exceptions are the CSDs of the fine-grained samples S-7-4 and S-12-4, which are highlighted in Fig. 8. The CSDs of these

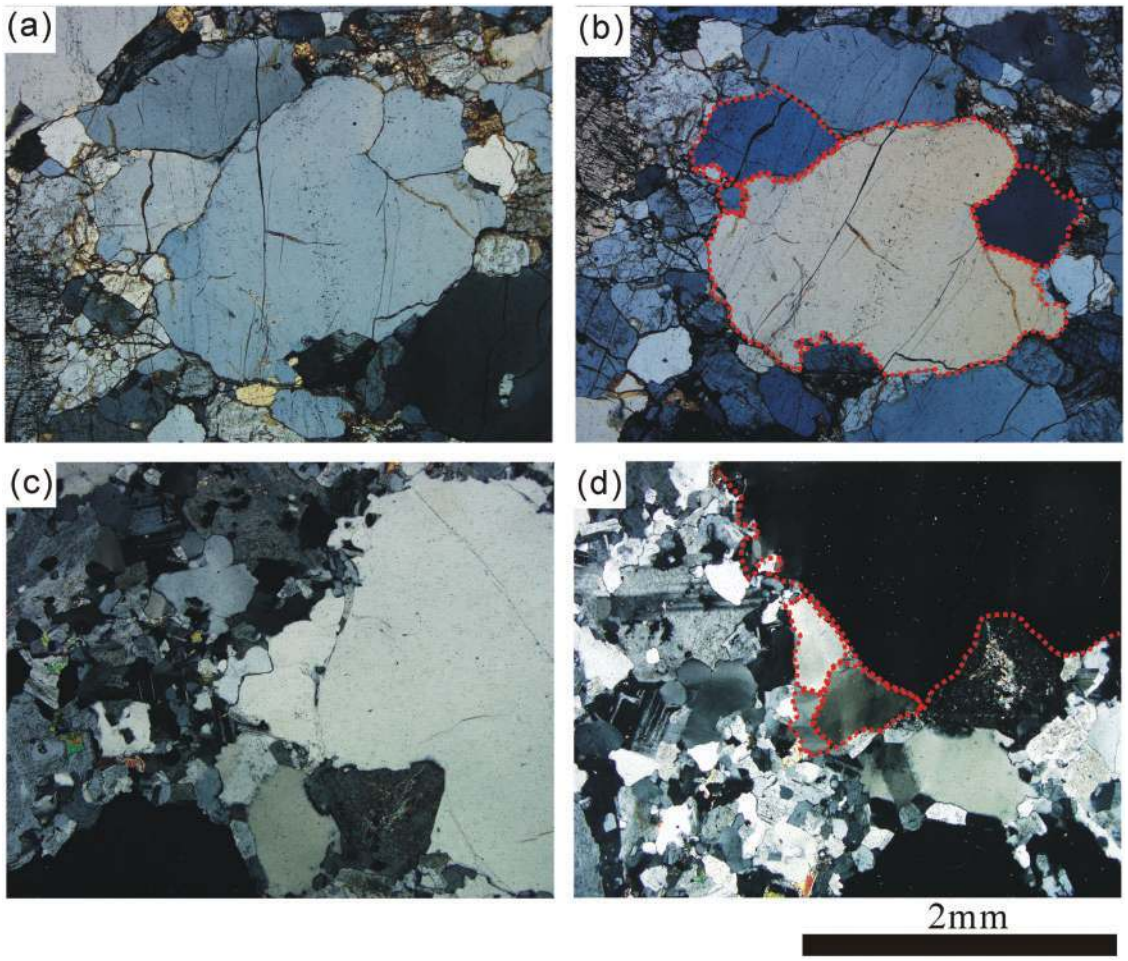

Fig. 6. Photomicrographs to illustrate how touching quartz crystals are separated by changing their interference color. In both (a) and (c) the touching crystals have the same interference color and separation is difficult; however, it becomes easier to outline each of the touching crystals when their interference color is changed by rotating the microscope stage.

two samples neither significantly turn down at smaller crystal lengths, nor show curved, concave-up shapes; they can therefore be called straight CSDs (S-CSD) (Higgins, 2006*b*).

To fully illustrate and understand the quantitative textural characteristics for all the samples, the CSD data have been divided into three groups; group 1 comprises the fine-grained samples (Fig. 8a); group 2 are the phenocrysts of the coarse-grained samples (Fig. 8c); group 3 comprises the groundmass of the coarse-grained samples (Fig. 8d).

A general fundamental and universal equation that uniquely relates CSD slope and intercept has been given by Zieg & Marsh (2002) and Marsh (2007) as

$$\ln(n^0) = 4\ln(S) - \ln(C) \quad (1)$$

where $\ln(n^0)$ is the intercept and S is the absolute value of the slope of the CSD. C is a modal normalization factor and can be obtained from the following equation (Zieg & Marsh, 2002):

$$N_T \bar{L}^3 = C^{-1} \quad (2)$$

where N_T and $\bar{L}$ are the total number and mean length of the crystals in the sample. When $N_T \bar{L}^3$ is compared with the observed modal abundance of quartz (X_{Qz}) in the samples from this study (Fig. 9a), there is a clear correlation:

$$N_T \bar{L}^3 = 0 \cdot 41 X_{Qz} = C^{-1}. \quad (3)$$

In Fig. 9b equations (1) and (3) are used to explore the Shanggusi quartz CSD data. All the samples have values of C in the range of 6–30, corresponding to X_{Qz} of 0·08–0·41.

The coarse-grained samples are all fairly uniform with 24–39% quartz crystals up to 4 mm long. The porphyritic texture is expressed as strongly curved and concave-up

Table 1: Textural parameters of the Shanggusi granite porphyry samples

Sample	Distance (m)	AR1	AR2	Number	AF	Roundness	Area (mm^2)	*R*	L_{max} (mm)	Vol. phase (%)	CSD volume (%)	Regression volume (%)	Intercept	Error (1σ)	Slope	Error (1σ)	CL	Total number (cm^{-3})	Goodness of fit (*Q*)
s-3-2	−25	1·82	2	693	2·7	0·6	204·9	1·21	1·10	21·0	22·0	24·09	5·54	0·12	−7·05	0·29	0·142	11200	0·0444
s-3-3	−25	1·82	1·89	679	31·3	0·6	211·3	1·22	1·12	22·3	22·1	25·83	5·75	0·15	−7·31	0·32	0·137	9830	0·0566
s-7-4	90	1·54	1·91	353	21·4	0·6	247·3	1·20	2·08	35·9	45·7	39·13	2·61	0·13	−3·14	0·15	0·318	3180	0·2788
s-7-5	96	1·54	1·91	535	11·1	0·6	235·6	1·26	1·87	27·9	34·2	32·95	4·27	0·15	−4·96	0·26	0·202	5610	0·6844
s-8	199	1·54	1·65	565	12·9	0·7	98·0	1·20	0·92	32·3	33·6	36·94	6·05	0·13	−7·39	0·35	0·135	22300	0·0531
s-12-1B	219	2	2·54	323	32·8	0·5	289·6	1·21	2·49	24·2	26·9	24·90	2·84	0·15	−3·54	0·19	0·282	2120	0·4648
s-12-2	219	1·67	1·87	442	12·5	0·7	32·9	1·22	0·57	30·5	31·9	34·19	7·66	0·15	−11·10	0·60	0·090	82800	0·6308
s-12-4	229	1·43	1·65	880	40·5	0·7	299·5	1·20	1·19	24·7	28·1	26·66	4·68	0·09	−5·91	0·20	0·169	10300	0·5143
s-6-1(W)	13	1·67	1·93	523	31·3	0·7	216·5	1·08	1·94	26·9	27·7	29·55	4·32	0·10	−4·97	0·19	0·201	9360	2E-06
s-6-1(G)	13	1·67		415		0·7	173·0	0·96	0·56	8·8	8·7	10·56	5·48	0·14	−8·60	0·46	0·116	11500	0·7941
s-6-1(P)	13	1·67	1·93	152	31·3	0·7	216·5	1·30	1·94	22·3	23·1	26·18	3·02	0·29	−3·70	0·33	0·270	969	0·3713
s-6-3(W)	38	1·43	1·64	1010	5·1	0·7	502·1	1·04	4·20	30·8	35·2	32·79	4·26	0·08	−4·95	0·14	0·202	6140	5E-06
s-6-3(G)	38	1·43		964		0·7	421·0	1·06	0·97	17·6	19·4	20·95	4·88	0·11	−6·48	0·25	0·154	6070	0·1426
s-6-3(P)	38	1·43	1·64	81	5·1	0·7	502·1	1·08	4·20	18·8	20·1	19·29	0·11	0·32	−2·00	0·21	0·500	152	0·2105
s-6-5(W)	43	1·67	2·11	732	59·6	0·7	317·3	1·11	2·32	32·3	36·3	33·66	4·04	0·10	−4·48	0·15	0·223	6410	1E-05
s-6-5(G)	43	1·67		682		0·7	317·3	1·06	1·27	22·6	23·8	25·25	4·41	0·12	−5·29	0·22	0·189	6380	0·479
s-6-5(P)	43	1·67	2·11	46	59·6	0·7	317·3	1·27	2·32	13·2	17·1	18·47	1·32	0·68	−2·64	0·47	0·379	120	0·9186
s-7-1(W)	52	1·43	1·64	533	27·8	0·7	389·9	1·02	4·58	39·1	43·4	39·59	3·29	0·11	−3·71	0·14	0·270	3870	0·0002
s-7-1(G)	52	1·43		483		0·7	389·9	0·88	0·97	11·0	12·5	14·13	3·93	0·14	−5·64	0·31	0·177	3640	0·0179
s-7-1(P)	52	1·43	1·64	81	27·8	0·7	389·9	1·12	4·58	30·7	33·0	35·47	0·20	0·35	−1·76	0·21	0·568	183	0·127
s-7-2(W)	69	1·67	1·97	566	37·3	0·7	347·4	1·11	4·26	31·9	34·4	33·66	3·78	0·11	−4·20	0·16	0·238	4290	0·0002
s-7-2(G)	69	1·67		530		0·7	347·4	1·04	0·98	14·3	14·5	18·36	4·38	0·16	−5·68	0·31	0·176	4090	0·7876
s-7-2(P)	69	1·67	1·97	71	37·3	0·7	347·4	1·21	4·26	20·8	22·4	25·51	0·88	0·43	−2·18	0·30	0·459	211	0·7801
s-7-3(W)	86	1·67	1·96	668	50·7	0·6	415·8	1·04	3·36	27·1	28·0	28·38	3·91	0·12	−4·61	0·18	0·217	4470	0·4631
s-7-3(G)	86	1·67		653		0·6	375·0	1·06	1·32	18·0	20·1	19·37	4·03	0·10	−5·23	0·19	0·191	4800	0·0527
s-7-3(P)	86	1·67	1·96	152	50·7	0·6	933·0	1·08	3·66	15·1	16·0	15·80	0·40	0·21	−2·21	0·15	0·452	163	0·1778
s-7-7A(G)	134	1·67		273		0·7	94·0	1·00	0·68	9·5	9·4	11·49	6·65	0·24	−11·30	0·80	0·088	14300	0·4045
s-7-7A(P)	134	1·67	1·72	175	42·9	0·7	949·0	0·98	3·19	16·2	16·0	16·76	0·02	0·21	−1·95	0·14	0·513	195	0·0587
s-7-8(W)	159	1·54	1·64	679	61·2	0·7	260·7	1·08	2·88	26·1	27·9	29·79	5·10	0·13	−6·26	0·27	0·160	8190	0·8838
s-7-8(G)	159	1·54		669		0·7	237·0	1·09	0·95	19·0	20·7	21·62	5·24	0·12	−6·91	0·28	0·145	9120	0·219
s-7-8(P)	159	1·54	1·64	47	61·2	0·7	870·6	1·09	3·09	9·6	11·5	13·30	−1·69	0·46	−1·38	0·23	0·725	35	0·2946
s-7-10A(W)	198	1·54	1·51	1090	49·4	0·7	341·7	1·12	2·56	33·5	34·3	34·33	4·92	0·08	−5·68	0·16	0·176	11300	0·0023
s-7-10A(G)	198	1·54		1061		0·7	300·0	1·14	0·98	24·5	25·0	27·80	5·30	0·09	−6·57	0·20	0·152	12900	0·9832
s-7-10A(P)	198	1·54	1·51	217	49·4	0·7	979·0	1·04	2·94	13·6	14·0	12·50	2·12	0·27	−3·63	0·26	0·275	239	0·3505
s-7-9(G)	179	1·54		321		0·7	93·0	1·18	0·88	20·7	22·4	24·98	6·00	0·24	−8·05	0·54	0·124	12800	0·6478
s-7-9(P)	179	1·54	1·74	126	4·8	0·7	873·0	1·03	3·39	9·5	11·0	9·10	1·10	0·34	−3·04	0·30	0·329	149	0·9756
s-9-1(W)	200	1·54	1·87	1077	19·6	0·7	361·5	1·06	2·75	24·1	27·0	25·74	5·24	0·08	−6·61	0·18	0·151	11700	1E-11
s-9-1(G)	200	1·54		1053		0·6	330·0	1·07	0·95	16·9	18·6	18·10	5·65	0·08	−8·00	0·23	0·125	13000	0·0042
s-9-1(P)	200	1·54	1·87	116	19·6	0·6	885·0	0·93	4·03	14·2	14·6	16·10	0·23	0·32	−2·16	0·21	0·463	117	0·4255
s-10-1(G)	203	1·82		352		0·7	164·0	1·07	0·95	13·7	12·4	13·70	5·08	0·14	−7·12	0·34	0·140	8490	0·0027
s-10-1(P)	203	1·82	1·77	123	35·1	0·6	858·0	0·96	3·93	15·0	13·8	16·20	0·02	0·23	−1·96	0·15	0·510	138	0·2561
s-11-1(G)	217	1·67		421		0·7	170·0	1·11	0·92	18·0	17·2	19·50	5·65	0·19	−7·70	0·42	0·130	7980	0·7099
s-11-1(P)	217	1·67	1·75	62	41·2	0·7	860·8	0·98	3·37	7·7	7·5	9·20	−0·16	0·44	−2·17	0·30	0·461	75	0·595

The eight samples at the top of Table 1 are fine-grained samples in this study. (W), (G) and (P) refer to whole crystals, groundmass and phenocrysts of quartz in each sample respectively. Distance, 0 m represents the location of the intrusion contact with the wall-rock on the west side; positive and negative numbers refer to the east and west side relative to the 0 m location respectively. AR1, average aspect ratio. AR2, average aspect ratio of the 40 largest crystals. Number, number of grains analyzed. AF, alignment factor. Roundness, average roundness of grains analyzed. Area, area of thin section analyzed. *R*, spatial distribution *R*-value. L_{max}, average of the four largest intersection lengths of each sample. Vol. phase, volume of quartz determined from the area of quartz in thin section. CSD volume, regression volume, intercept, slope, CL (characteristic length), total number, and goodness of fit are calculated using *CSDCorrections 1.38*. It should be noted that slope and intercept for whole crystals of each sample (W) do not have much physical significance, but other parameters might be meaningful. The 'goodness of fit', *Q*, is a parameter that describes the quality of fit of the linear regression (see text for details).

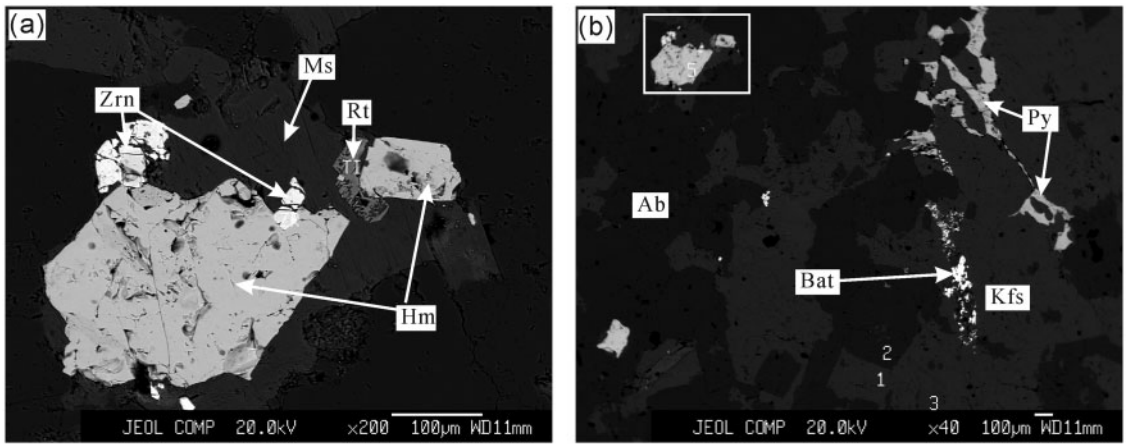

Fig. 7. Back-scattered electron images showing representative accessory mineral characteristics. (a) Magnified view of the white rectangle in (b). Ab, albite; Bat, bastnasite; Hm, hematite; Kfs, potassium feldspar; Py, pyrite; Rt, rutile; Zrn, zircon.

CSDs. Because it is difficult to parameterize curved CSDs, here the CSD is considered as the sum of two straight CSDs, as done by Higgins (1996), but without the implication that the texture was produced necessarily by mixing. CL is about 0·27–0·73 mm for the population of phenocrysts (group 2) and 0·09–0·19 mm for the population of groundmass crystals (group 3) (Table 1). The intercept varies from −1·69 to 3·02 for the population of phenocrysts (group 2) and from 4·03 to 6·65 for the population of groundmass crystals (group 3). The characteristic length (CL) of the fine-grained samples (group 1) varies from 0·09 to 0·28 mm and intercept ranges from 2·61 to 7·66. The volumetric proportions of quartz in the fine-grained samples (group 1) have a limited range of 21–36%. The maximum crystal size is 2·5 mm.

A plot of CSD characteristic length vs volume phase proportion (see Higgins, 2002*a*) highlights three distinct groups for all the quartz crystals (Fig. 10a). Plots of L_{max} against CSD slope are shown in Fig. 10b. It should be noted that L_{max} is measured (in mm) as the average of the four largest grains from the crystal population of each sample (e.g. Boorman *et al.*, 2004; O'Driscoll *et al.*, 2007, 2008). The two strong positive correlations of L_{max} against CSD slope suggest that the group 1 and group 2 CSD data represent two distinct crystal populations, which is consistent with their different emplacement stages in the field.

Figure 11 presents the spatial variation of slope, intercept, L_{max}, and total number of crystals (per cm^3) as a function of distance in the intrusion. There is no obvious regular variation of these parameters for group 1 and group 2. None the less, the L_{max} and slope of group 3 in the margins of the intrusion are larger than those in the center, and the intercept and total number of crystals show opposite characteristics. The representative photomicrographs of the margins and the center of the intrusion that are shown at the top of Fig. 11 qualitatively indicate that the groundmass at the center of intrusion is finer grained, with a more rapid cooling history.

SDP plots

Crystal spatial distribution can be random, ordered or clustered, as quantified by the *R*-value method applied to a thin section (Jerram *et al.*, 1996). For example, in Fig. 12, populations of grains plotting above the random distribution line (RSDL) are ordered, whereas populations below this line are clustered. The trends for grain distributions that have undergone different degrees of size sorting, mechanical compaction (simple grain rearrangement), deformational compaction or overgrowth have been determined (Jerram *et al.*, 1996), and are shown as vector arrows in Fig. 12. The vector for sorting shows the trend expected for increasingly better size sorting, and the overgrowth vector reflects the movement of grain centers with grain overgrowth of neighboring grains. The mechanical compaction trend reflects an increase in *R*-value coupled with a decrease in matrix abundance as grains undergo simple re-ordering and move into contact with each other in response to loss of interstitial liquid. The deformational compaction trend results from a decrease in *R*-value as the pure shear deformation of initially spherical grains causes the grain centers to move apart in a plane normal to the principal stress, along with a further decrease in matrix abundance (Jerram *et al.*, 1996).

The spatial distribution data from the Shanggusi samples generally show a negative trend in Fig. 12. The *R*-value of group 2 has a very broad variation, and changes from a clustered to a more random distribution. The negative trend seen in most of the data for group 3 can be the result of variable degrees of overgrowth and/or mechanical compaction. The scattered negative trends of group 1 and group 2 might result from more complex processes and are discussed in more detail below.

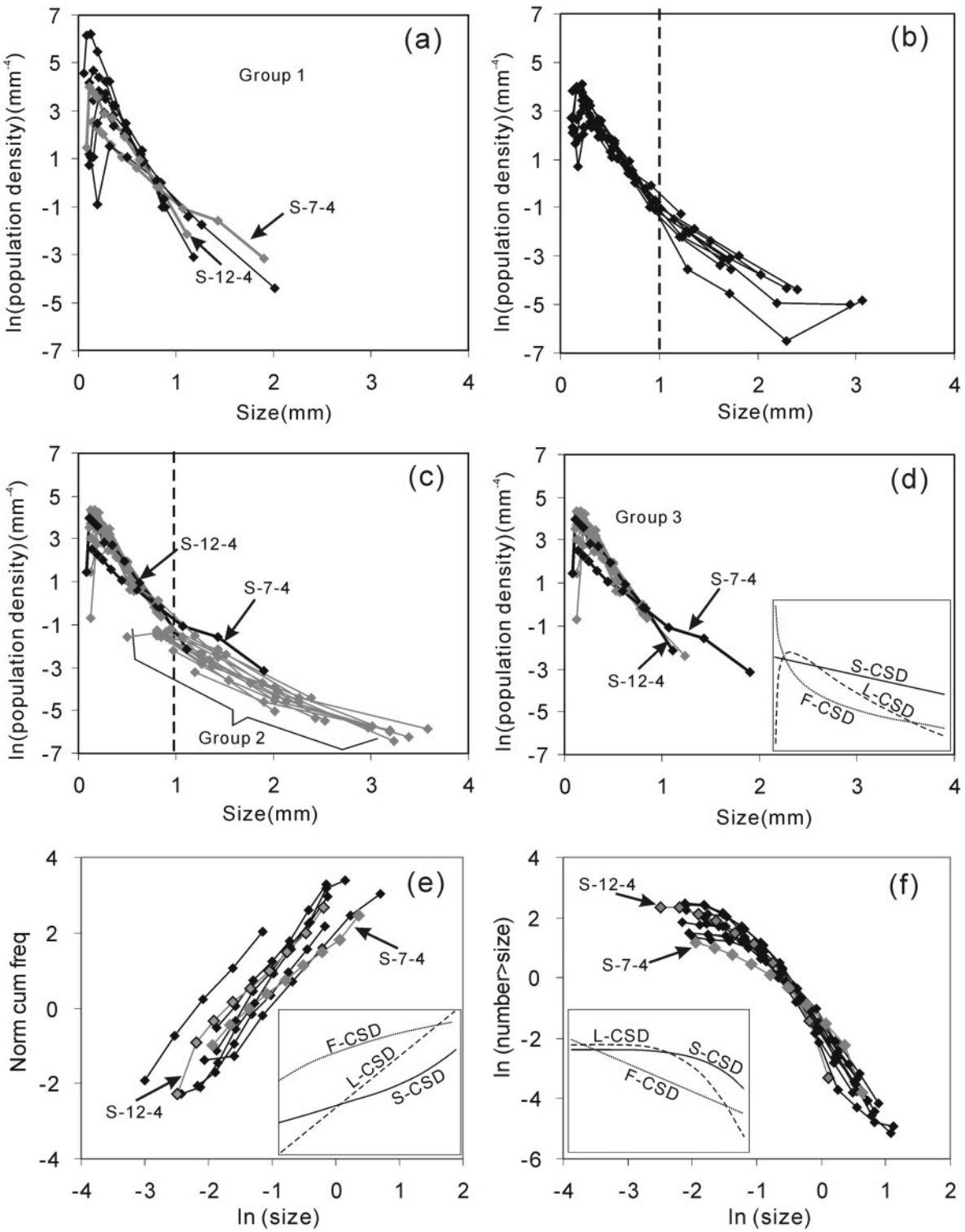

Fig. 8. Quartz CSDs for all the studied samples. (a) Fine-grained samples, including six samples from the granite dyke (group 1) and two samples (labelled) from the granite porphyry. (Note the sequence of progressively shallower right-hand parts to the CSDs observed for group 1 samples.) (b, c, d) Coarse-grained samples of the granite porphyry. The groundmass and phenocryst are simultaneously considered in (b) and are separated in (c). The CSDs with large size range and shallower slope in (c) are phenocryst data (group 2). (d) Groundmass CSDs (group 3). (e) Cumulative distribution function diagrams showing log-normal CSDs for group 1 samples. (f) Bi-logarithmic cumulative size diagram. The schematic inset diagrams in (d)–(f) show three different theoretical CSD models.

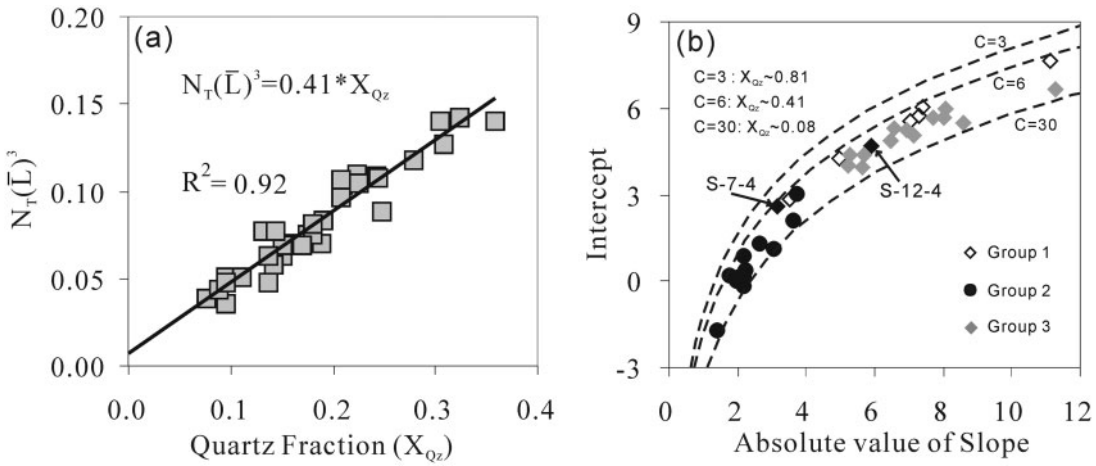

Fig. 9. (a) Relationship between $N_T\bar{L}^3$ and X_{Qz}. (b) Comparison of measured and predicted CSD slopes and intercepts. Predicted curves are from equation (1); measured values are from Table 1.

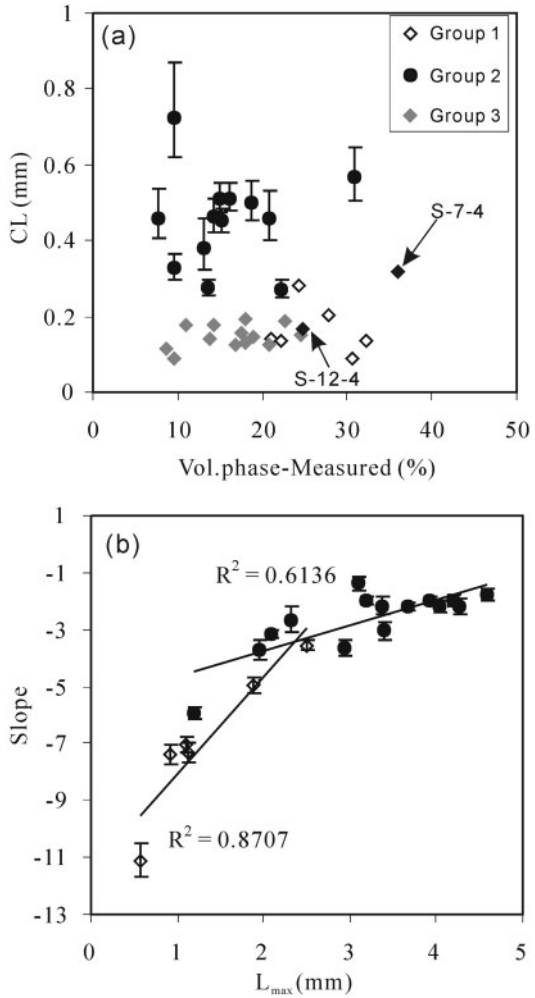

Fig. 10. (a) Plot of characteristic length (CL) vs measured volume phase proportion for all the studied samples. (b) Plot of slope vs L_{max} for group 1 and group 2. R^2 values indicated. The errors for CL and slope are indicated where these are larger than the symbol size.

The progressive deformation of initially spherical grains will produce grains that have increasingly higher aspect ratios and become more similar to tabular grains in shape. Hence, one would expect *R*-value to show a negative correlation when plotted against the aspect ratio if deformation were the cause of the positive trend in Fig. 13b. In contrast, if the trend were the result of better sorting, one might expect the *R*-value to correlate positively with CSD slope (Fig. 13a); well-sorted samples should have a more uniform size distribution and hence a flatter slope. Plots of *R*-value against CSD slope show a relative modest negative correlation for group 2 and no clear correlation trend for the other groups (Fig. 13a). Plots of *R*-value against aspect ratio show a slightly positive correlation for group 2 (Fig. 13b). Hence, the variation trends of *R*-value for all the samples mainly result from variable degrees of overgrowth and/or mechanical compaction.

Alignment factor

Data for the alignment factor (AF) in all of the samples are presented in Table 1. The AF value of group 1 and group 2 ranges from 2·7 to 40·5 and from 4·8 to 61·2 respectively. Therefore, there is a higher degree of alignment of the long axes of the phenocrysts in group 2. If the higher degree of alignment results from deformational compaction, plots of aspect ratio against alignment factor would show a positive correlation. However, such a trend is not observed in Fig. 14a. Plots of the volume fraction (group 1 and group 2) against alignment factor show a noisy negative correlation (Fig. 14b). This cannot be due to deformational compaction, which would result in an increase of the volume fraction (group 1 and group 2) with increasing alignment factor. In addition, there is no clear correlation trend between the AF value and bulk-rock trace element content (e.g. $\sum$REE) (Fig. 15), suggesting

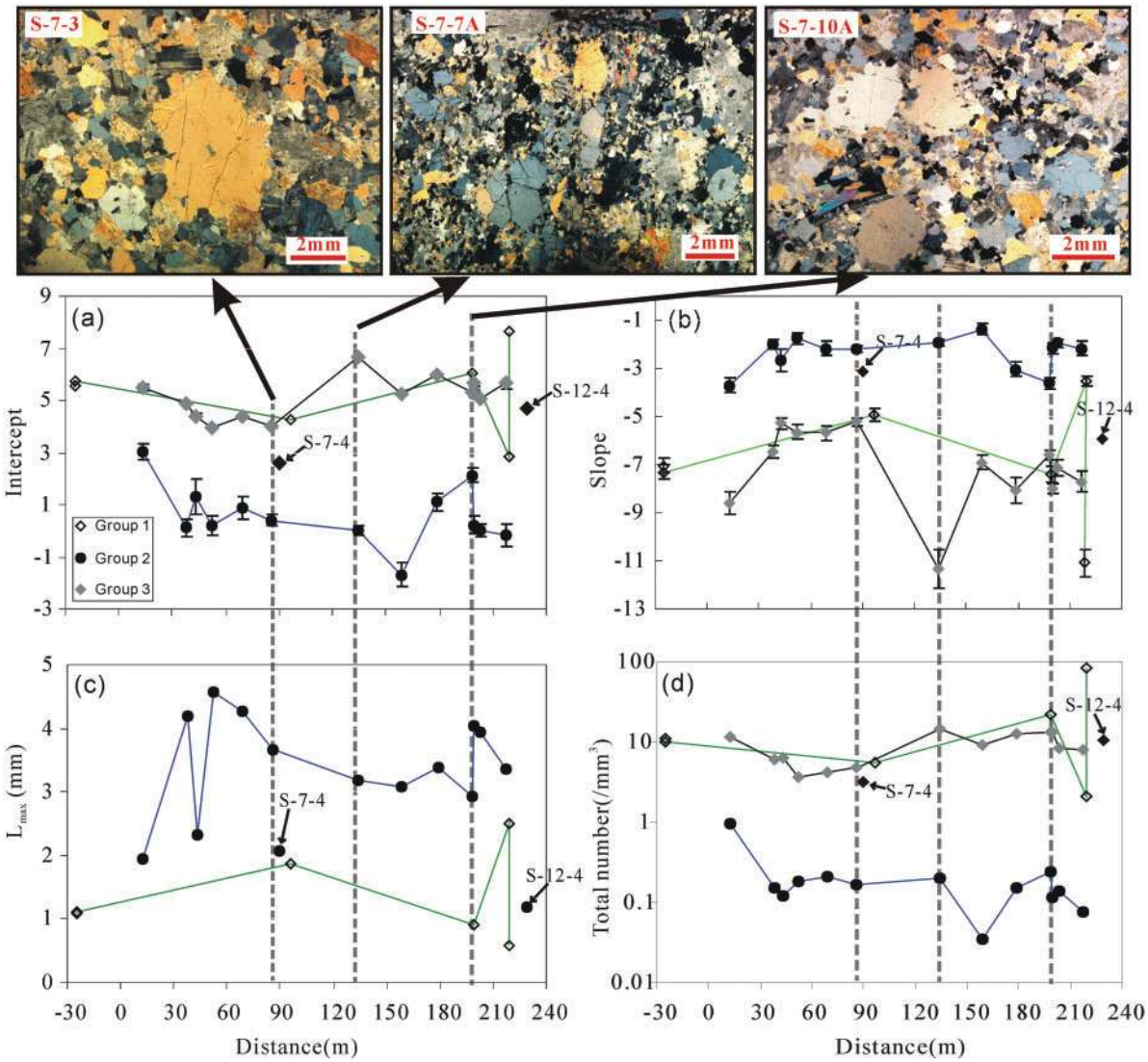

Fig. 11. Textural data plotted as a function of horizontal distance within the intrusion; 0 m represents the location of the intrusion contact with the wall-rock on the west side; positive and negative numbers refer to the east and the west side relative to the 0 m location respectively. The exact location of each sample is shown in Fig. 2. The photomicrographs at the top of the figure illustrate the textural characteristics of the samples. It should be noted that the center of the intrusion has a finer-grained groundmass than that at the margins.

that magmatic flow, although it can explain the alignment of the phenocrysts, is not responsible for the fractionation of trace elements during the solidification process.

Geochemical characteristics

Major element compositions

Despite the large variation in texture, the major element composition of the Shanggusi granite porphyry is relatively homogeneous (Table 2). The rocks are highly siliceous (SiO_2 = 74·9–79·5%) and are enriched in alkalis ($K_2O + Na_2O$ = 8·4–9·2%). They have minor amounts of MgO, CaO, MnO, TiO_2 and P_2O_5, and low abundances of Fe_2O_3 (<1·97%) and FeO (<1·15%). Al_2O_3 contents vary from 10·1 to 14·0%. F abundances vary from 49 to 1349 ppm. Cl abundances vary from 9 to 555 ppm. Figure 16 shows co-variation diagrams between SiO_2 and a range of major and minor oxides; the fine- and coarse-grained samples show remarkably similar major element compositions. Plots of Al_2O_3, MgO and Na_2O against SiO_2 show weak negative correlations. SiO_2 vs Cl and K_2O define relatively modest positive correlations, and a very noisy correlation when plotted versus F (Fig. 16). These weak correlations are probably due to the limited variation range in SiO_2. However, it generally seems that the variation of major elements is related to varied degrees of fractional crystallization of Na-plagioclase.

Trace element compositions

The rare earth element (REE) patterns for all the samples are characterized by enriched light REE (LREE), slightly enriched heavy REE (HREE) and pronounced negative Eu anomalies (Eu* = 0·33–0·67) (Fig. 17a, Table 3). In multi-element patterns, all the samples show characteristic negative anomalies in Ba, Sr and Ti, and positive anomalies in Th, U, Pb and Hf (Fig. 17b).

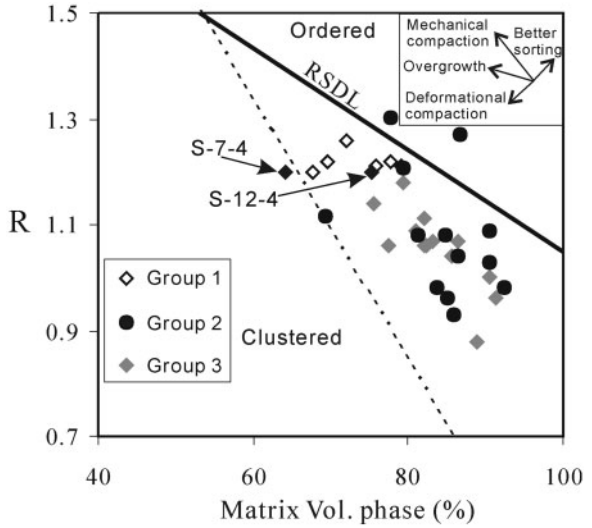

Fig. 12. *R*-value vs matrix volume phase (%) for all the studied samples. RSDL is a line for the random distribution of spheres of differing modal abundance (Jerram *et al.*, 1996). Data above RSDL indicate an ordered grain distribution whereas those below it have a clustered grain distribution. The vectors indicate expected changes caused by different processes (Jerram *et al.*, 1996). The distribution of crystals plotting above the dashed line has a non-touching framework of crystals (Jerram *et al.*, 2003).

Because feldspar and quartz are the major rock-forming minerals in the Shanggusi granite porphyry, Sr, Ba and Eu can be considered as compatible elements and Th and REE as incompatible elements for all the samples. Plots of Eu* vs Sr and Ba show no clear correlation for the fine-grained samples (Fig. 18). Plots of Eu* vs Sr, Ba and CaO/Al_2O_3 show a modest positive correlation for the coarse-grained samples (Fig. 18), which are in principle in agreement with fractionation of feldspar. However, the observed slightly positive correlations of Eu* vs La and lack of correlation of Eu* vs Th (Fig. 18) are inconsistent with typical feldspar fractional crystallization trends. In addition, plots of Sr vs REE, Ba vs Th and CaO/Al_2O_3 vs La show relatively good positive correlations (Fig. 18), implying that the assumed compatible elements Ba and Sr, and the CaO/Al_2O_3 ratio, display the behavior of incompatible elements, which indicates that fractionation of these trace elements is not the result of fractional crystallization of feldspar. Furthermore, there is no correlation between Eu* and quartz volume fraction (Fig. 18), indicating that the variation of quartz volume fraction does not control the fractionation of these trace elements. In summary, the negative Eu anomalies and the trace element fractionation might not mainly result from the fractional crystallization of the major rock-forming minerals (quartz and feldspars). The negative Eu anomalies may instead be a characteristic of the source region, reflecting the impact of residual plagioclase. The fractionation of trace elements might also be controlled by other magmatic processes; this will be discussed together with quantitative textural analysis below.

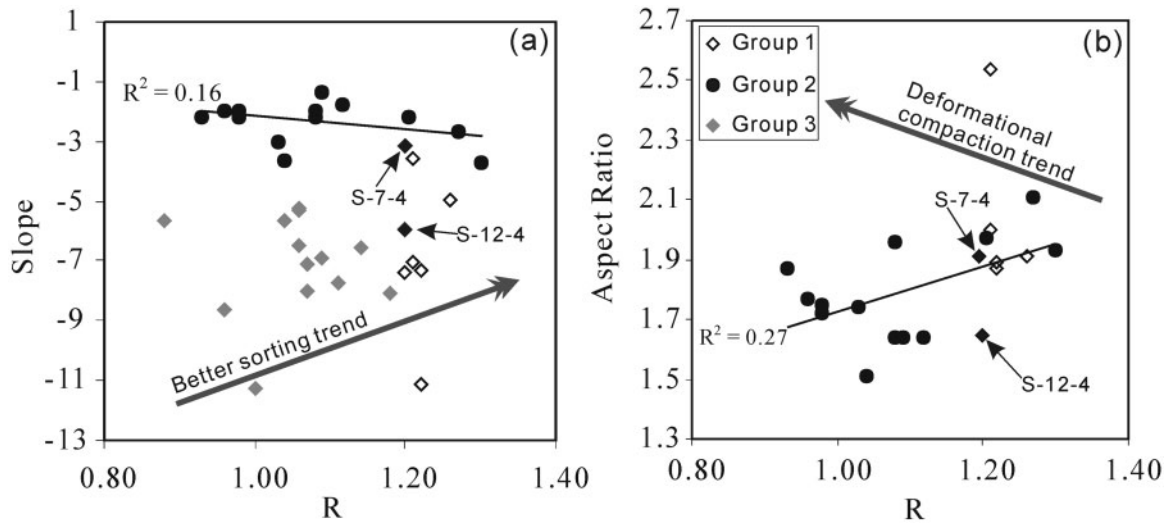

Fig. 13. (a) Plot of CSD slope vs *R*-value for all the samples. (b) Plot of aspect ratio vs *R*-value for group 1 and group 2. It should be noted that the aspect ratios used here are averages of the major/minor axes of the 40 largest crystals in each sample (AR2 in Table 1) as larger crystals are more sensitive to deformational compaction. Group 3 is not considered here.

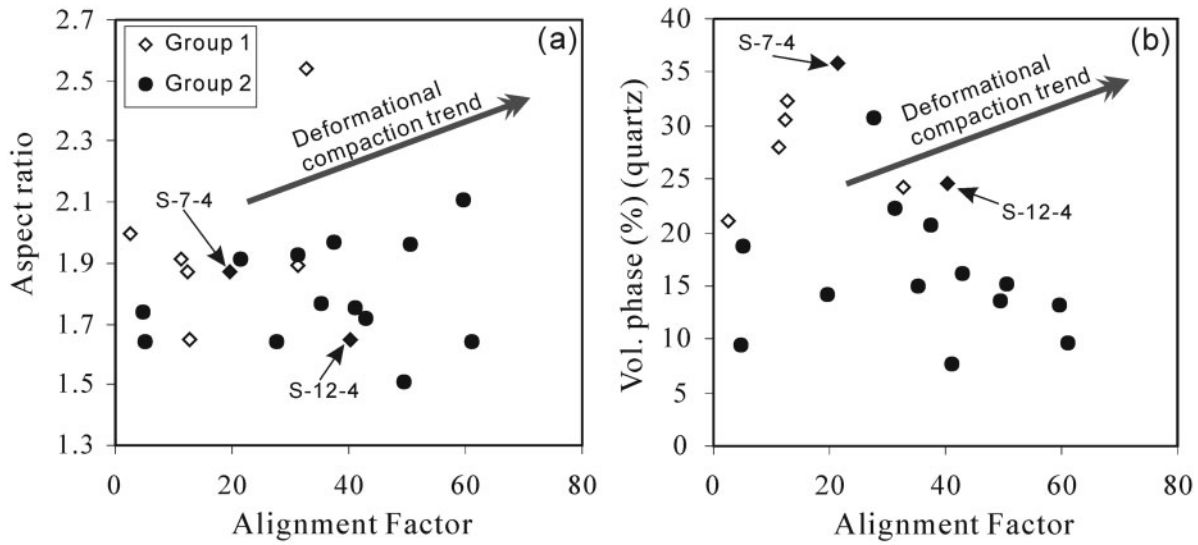

Fig. 14. (a) Plot of aspect ratio vs alignment factor for group 1 and group 2. The aspect ratios used here are an average of the major/minor axes of the 40 largest crystals in each sample (AR2 in Table 1). (b) Plot of volume phase (%) vs alignment factor for group 1 and group 2.

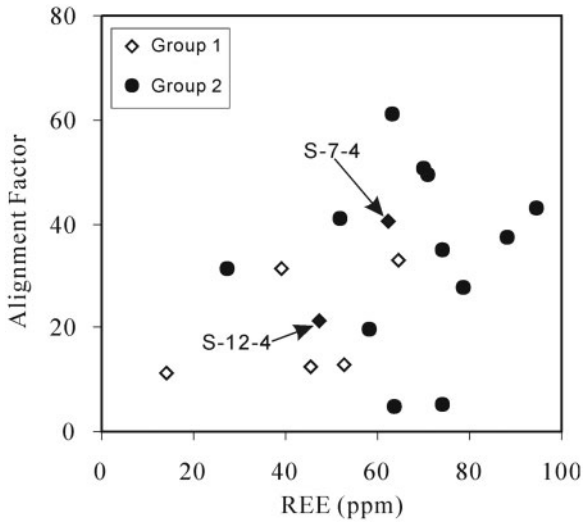

Fig. 15. Plot of alignment factor vs bulk-rock REE content for group 1 and group 2.

DISCUSSION

Crystal nucleation and growth

The data for SDP and AF suggest that the textural features of the Shanggusi granite porphyry can generally be regarded as the result of simple crystal nucleation and growth processes. Magmatic flow and mechanical compaction of crystals, as discussed above, did not significantly affect the original nucleation and growth of quartz. Therefore, the CSD data are appropriate to explore the fundamental aspects of crystal nucleation and growth during the progressive solidification of the intrusion. The CSDs of group 1 and group 3 exhibit a general concave-down shape, which means that small crystals are deficient when compared with the linear CSDs observed in other systems (e.g. Mock *et al.*, 2003). Concave-down CSDs for quartz crystals have been reported for silicic systems in several recent studies (e.g. Bindeman, 2003; Stemprok *et al.*, 2008; Inanli & Huff, 2009). Bindeman (2003) and Inanli & Huff (2009) concluded that concave-down log-normal CSDs are a general result of surface-controlled, size-dependent growth, with a minor textural coarsening component; they are an intrinsic property of near-equilibrium systems, such as large-volume, near-eutectoid, silicic magma bodies. Stemprok *et al.* (2008) proposed that the small-size fraction of quartz crystals is eliminated by subsolidus annealing. However, one controversy surrounding these earlier studies involves the interpretation of log-normal CSDs and whether they can be produced as a result of size-independent (constant) crystal growth. Eberl *et al.* (2002) demonstrated that log-normal CSDs cannot be generated or maintained by size-independent crystal growth based on the population-balance modeling equation. However, a deficit of small crystals may also be produced by other processes. Marsh (1998) suggested that, in a hypothetical closed system, the diminishing liquid fraction during the last stages of crystallization could cause a pronounced decrease in the CSD at the smallest crystal sizes. Although such a process can produce a single concave-down CSD, it cannot produce the sequence of progressively shallower right-hand parts to the CSDs observed here for group 1 and group 3 and in many other studies (e.g. Higgins, 1998, 1999, 2002*a*; O'Driscoll *et al.*, 2008; Inanli & Huff, 2009). In addition, it

Table 2: Whole-rock major element, Cl and F compositions of the Shanggusi granite porphyry samples

Sample:	S-6-1	S-7-3	S-7-4	S-7-5	S-7-8	S-8	S-9-1	S-7-10A	S-3-3	S-6-3	S-7-1	S-7-2	S-7-7A	S-7-9	S-10-1	S-11-1	S-12-1	S-12-2	S-12-4
SiO_2	75·71	75·63	75·98	76·38	75·45	79·50	75·78	76·26	74·91	76·32	75·79	75·24	77·77	77·22	77·24	77·80	77·34	75·51	77·43
Al_2O_3	13·37	13·15	13·45	13·28	13·23	11·55	13·09	13·07	14·04	11·20	11·01	11·53	10·06	11·01	10·85	10·89	11·11	12·47	11·46
Fe_2O_3*	0·73	0·63	0·45	0·06	0·59	0·16	0·53	0·58	0·45	1·91	2·47	2·19	2·26	1·90	2·04	1·76	1·32	1·47	1·43
MgO	0·07	0·15	0·11	0·07	0·11	0·03	0·11	0·11	0·07	0·10	0·09	0·11	0·07	0·06	0·08	0·06	0·03	0·02	0·01
CaO	0·29	0·42	0·37	0·33	0·62	0·20	0·35	0·32	0·55	0·53	0·51	0·47	0·52	0·42	0·41	0·51	0·43	0·25	0·29
Na_2O	4·43	4·26	4·85	4·74	4·74	4·17	4·36	4·63	5·66	4·10	3·92	4·00	3·25	4·39	3·87	3·99	3·85	4·46	4·44
K_2O	4·75	4·74	4·15	4·40	4·26	4·19	4·72	4·19	3·38	4·83	4·67	4·39	5·15	4·41	4·81	4·66	5·10	5·01	4·35
MnO	0·02	0·03	0·09	0·01	0·03	0·01	0·01	0·01	0·03	0·27	0·14	0·33	0·03	0·03	0·08	0·04	0·01	0·14	0·02
P_2O_5	0·01	0·03	0·02	0·01	0·02	0·01	0·02	0·02	0·02	0·03	0·02	0·03	0·03	0·02	0·03	0·02	0·01	0·02	0·01
TiO_2	0·04	0·06	0·04	0·01	0·03	0·00	0·04	0·04	0·02	0·07	0·07	0·08	0·09	0·06	0·07	0·06	0·06	0·04	0·03
LOI	0·51	0·34	0·31	0·24	0·40	0·20	0·35	0·32	0·21	0·48	1·05	1·36	0·51	0·30	0·34	0·10	0·50	0·45	0·35
H_2O^+	0·03	0·26	0·20	0·09	0·17	0·05	0·05	0·07	0·10	0·38	0·93	1·24	0·27	0·28	0·21	0·10	0·28	0·31	0·29
Total	99·93	99·42	99·82	99·52	99·47	100·01	99·35	99·56	99·32	99·83	99·74	99·73	99·74	99·83	99·81	99·79	99·76	99·84	99·83
FeO	0·09	0·16	0·10	0·10	0·06	0·11	0·04	0·09	0·19	0·90	0·45	0·35	1·10	1·10	1·00	1·00	0·75	1·15	1·15
Cl	17	33	28	18	17	9	34	26	26	128	88	43	555	347	388	290	406	187	135
F	180	180	1349	1019	941	941	156	1149	563	1226	870	549	613	643	562	1073	478	129	49

Fe_2O_3*, total iron. Oxides and LOI are in wt %; Cl and F are in ppm.

has been shown by experiment that in synthetic silicic melts quartz cannot coarsen measurably if its initial size is around a millimeter over geological timescales; however, textural coarsening may be very active at the end of nucleation events and result in the consumption of a significant proportion of crystalline nuclei (Cabane *et al.*, 2001).

Textural coarsening is also known as Ostwald ripening, textural maturation and equilibration, crystal ageing and annealing (e.g. Cashman & Ferry, 1988; Marsh, 1988; Boudreau, 1995; Elliott *et al.*, 1997; Higgins, 1998, 1999; Higgins & Roberge, 2003). This process occurs because small grains have a higher surface energy per unit volume than do larger grains. Therefore, crystals smaller than a critical size will dissolve and 'feed' the growth of larger crystals to minimize the energy of the system. This process can occur only when a crystal is held at a temperature close to its liquidus for a long period of time. Under these conditions, the nucleation rate is zero, but the growth rate is high for crystals larger than the critical size. This does not necessarily mean that the temperature is held constant, just that the undercooling remains small and the temperature is above the solidus. Several models have been proposed to account for textural coarsening processes (Lifshitz & Slyozov, 1961; Wagner, 1961; DeHoff, 1991; Simakin & Bindeman, 2008). Among these models, the Communicating Neighbours (CN) model has been successfully applied to plutonic rocks by Higgins (1998); this model is better than the Lifshitz-Slyozov-Wagner (LSW) model and can produce CSDs that are consistent with natural examples. However, both the CN and LSW coarsening models are for constant temperature, which might be unlikely in most magma chambers. A new coarsening model has been proposed more recently by Simakin & Bindeman (2008) and Mills *et al.* (2011) that takes into account such temperature variations. These researchers have shown that a time-series of multiple dissolution–reprecipitation episodes generates concave-downward CSDs and these results fit well with experimental and natural observations of the common concave-down CSDs in silicic igneous rocks. This might amplify the CN coarsening processes and the two might not be easily distinguishable. In the simplest CN coarsening models the system is closed and the volumetric proportion of the phase is constant; however, the quartz volume in the samples from the Shanggusi porphyry that have experienced the textural coarsening has changed more than 10%. Hence, textural coarsening might be an open-system process, reflecting transfer of material via a liquid phase that can migrate into or out of a rock.

Origin of curved CSDs

Although it is generally recognized that porphyritic textures are very common in granites, quantitative textural analysis has not been widely applied (see Higgins, 2006*a*), and further work is needed to investigate exactly which physical processes it reflects. The curved CSDs of the coarse-grained samples display F-type CSD characteristics

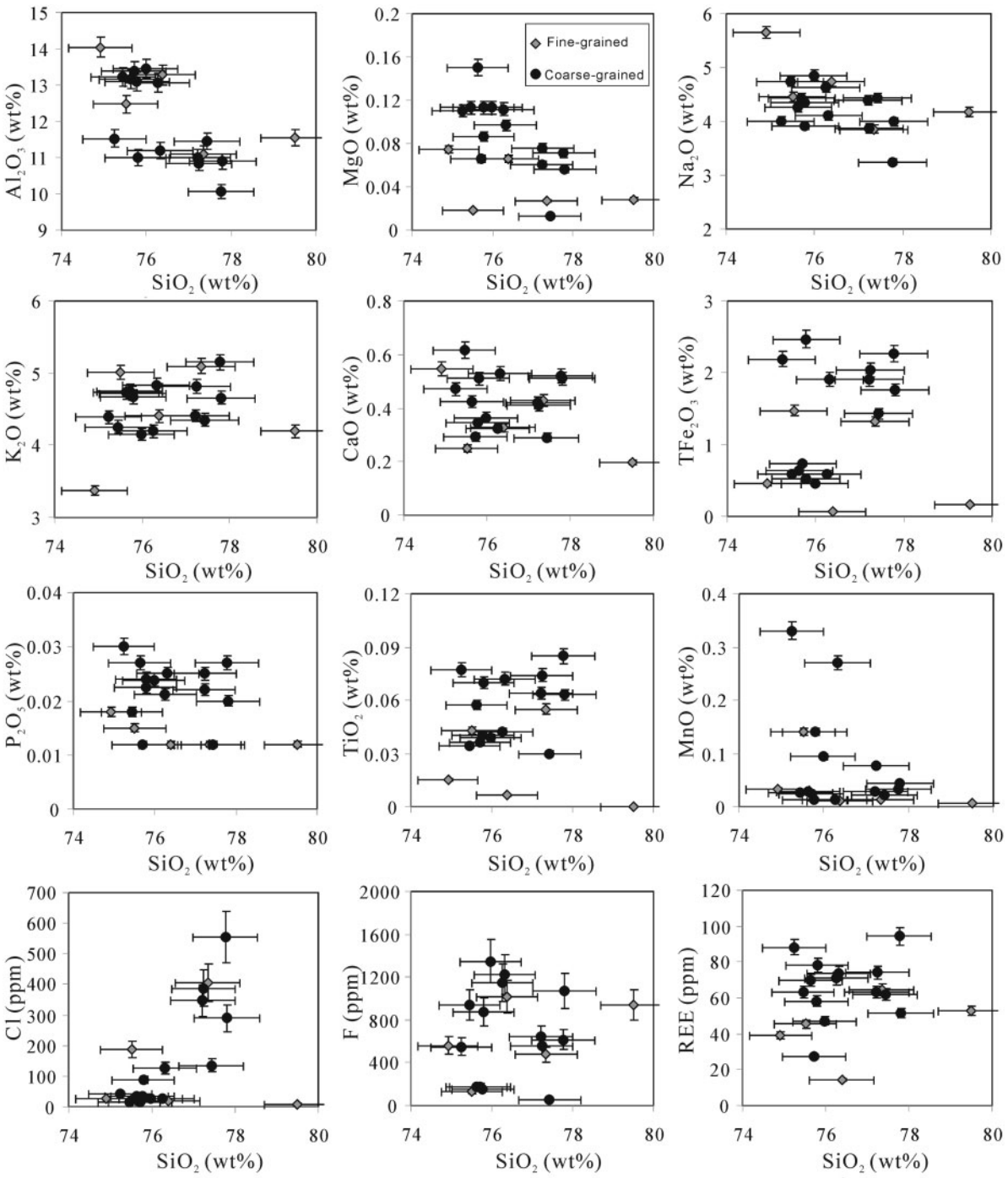

Fig. 16. Major element oxide vs SiO_2 variation diagrams for the fine- and coarse-grained samples.

as noted above. Several models have been proposed to explain F-type CSDs. Armienti *et al.* (1994) first proposed that crystallization within several different cooling regimes, such as a magma chamber and a conduit, could be responsible for F-type CSDs. Marsh (1998) suggested that a change of CSD slope can be affected by nucleation rate. Kinked CSDs may record sudden changes in nucleation rate. However, F-type CSDs may also result from the mixing of magmas with two different S-type CSDs (Higgins, 1996) or periods of textural coarsening in a magma chamber (Higgins & Roberge, 2003). Fractal size distributions (F-type CSDs) have also been considered to

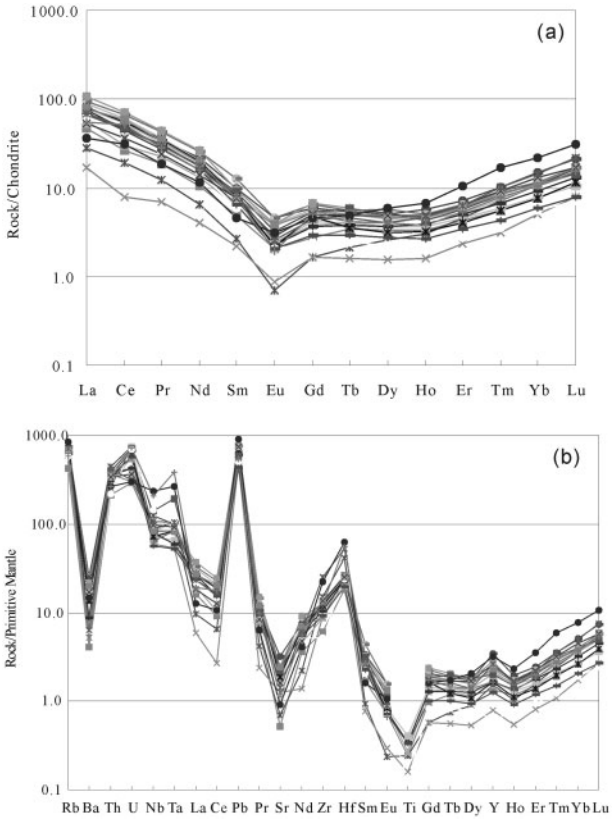

Fig. 17. (a) Chondrite-normalized REE patterns for the Shanggusi granite porphyry. (b) Primitive mantle-normalized trace element patterns of the Shanggusi granite porphyry. Normalizing values are from Sun & McDonough (1989).

result from crystal fragmentation (e.g. Marsh, 1998; Bindeman, 2005; Gualda & Rivers, 2006). However, the vast majority of the quartz phenocrysts in the Shanggusi porphyry are euhedral or subhedral, indicating that fragmentation processes are not significant. Therefore, the curved CSDs observed for the coarse-grained samples in this study are more likely to result from two different cooling regimes. Pamukcu *et al.* (2012) have demonstrated that the phenocrysts of quartz and feldspar in a silicic magma body represent crystallization in the deep magma chamber, whereas the fine-grained groundmass represents the final quenching process. The resorption of some quartz phenocrysts might be the result of ascent of phenocryst-bearing granitic magma under H_2O-undersaturated conditions (e.g. Blundy & Cashman, 2001; Stemprok *et al.*, 2008). In addition, a drop in pressure during adiabatic ascent of the magma may explain the resorption of perthite, as this ascent process may bring the temperature of an H_2O-undersaturated magma closer to its liquidus temperature. The overgrowth of perthite is probably due to the expansion of the stability field of alkali feldspar at the expense of quartz in the Qz–Ab–Or–H_2O system. Hence, the highly porphyritic texture, homogeneous bulk-rock major element and major rock-forming mineral compositions also support the suggestion that the kinked CSDs record sudden changes in nucleation rate rather than magma mixing.

Heterogeneity of textural and chemical characteristics

Combined with the relative homogeneous chemical composition of the major rock-forming minerals, the correlation between whole-rock major and trace elements, and quantitative textural analysis indicate that chemical fractionation across the profile of the Shanggusi granite porphyry is not mainly directly controlled by fractional crystallization, magma mixing, magma flow or mechanical compaction. The significant fractionation of minor and trace elements may be due to variations in the modal abundance of accessory minerals, such as apatite, zircon, rutile and rare earth minerals, as these minerals typically show very strong compatibility for almost all trace elements (Rollinson, 1993). During the magma solidification process, the trace elements that are typically concentrated in accessory minerals might be present in a fluid phase during major rock-forming mineral crystallization processes. The migration and convection of such fluids may influence the fractionation of trace elements. Plots of REE vs P_2O_5, TiO_2 and ($TFe_2O_3 + MgO + CaO$) show positive correlations for the coarse-grained samples, with the fine-grained samples plotting along the same variation trends (Fig. 19), suggesting that these minor elements may have behaved incompatibly. In addition, the positive trends of H_2O^+ vs REE, $TFe_2O_3 + MgO + CaO$, and Cs may also result from the migration and heterogeneous distribution of hydrous fluids (Fig. 19).

Fluids, characterized by low viscosity and density, migrate easily and have long been proposed as an effective medium for the transportation of various chemical components in magmatic systems, giving rise to differentiation and diversification of the resultant magmas (e.g. Boudreau *et al.*, 1986; Keppler & Wyllie, 1990; Wilkinson *et al.*, 1996; Webster, 1997; Ferlito & Lanzafame, 2010). At present, however, knowledge of the fluid–melt partitioning of trace elements is only fragmentary, and the data are inconsistent (e.g. Borchert *et al.*, 2010, and references therein). Another challenging aspect in understanding fluid-induced magmatic differentiation is that fluids can easily change their composition when they interact with melts, crystals or other fluids. This makes it difficult to identify the behaviour of fluids in a magmatic system. The correlations shown in Fig. 19 may suggest that the fluids in the Shanggusi intrusion are hydrous. Because fluid-bearing melts typically have lower solidus temperatures than equivalent dry melts, the heterogeneous distribution of fluids would give rise to variations in the degree of undercooling in the magma chamber, which differs from that

Table 3: Whole-rock trace element compositions of the Shanggusi granite porphyry samples (ppm)

Sample:	S-9-1	S-8	S-7-9	S-7-8	S-7-7A	S-7-5	S-7-4	S-7-3	S-7-2	S-7-10A	S-7-1	S-6-3	S-6-1	S-3-3	S-12-4	S-12-2	S-12-1	S-11-1	S-10-1
Sc	5·06	3·65	8·40	4·22	6·34	2·17	4·50	4·87	6·74	3·92	6·31	6·37	6·88	3·63	7·66	11·70	5·78	6·18	5·65
Cr	4·07	3·02	9·65	3·64	8·81	4·07	3·17	4·35	8·17	3·68	7·74	9·31	3·77	3·75	7·99	9·19	8·18	10·70	9·31
Co	0·12	0·10	1·00	0·23	1·13	0·14	0·17	0·69	0·83	0·29	0·59	1·24	1·09	0·27	1·12	1·38	1·01	1·13	1·19
Ni	1·26	0·83	1·17	0·92	1·01	1·18	0·77	1·67	1·28	2·89	0·95	1·42	1·04	0·88	1·65	2·23	1·30	1·20	1·19
Cu	30·5	3·6	30·0	9·1	11·6	3·7	4·0	4·4	13·5	15·9	4·1	4·9	25·9	3·9	16·5	12·4	8·6	16·1	4·6
Zn	29·7	12·7	28·3	34·6	38·2	17·3	41·0	36·4	31·0	23·1	31·6	71·8	22·3	21·8	49·2	38·1	27·9	45·3	27·5
Ga	26·9	29·4	23·5	29·9	21·8	29·8	28·5	26·8	23·0	26·6	22·8	22·9	31·3	30·5	29·4	32·6	25·4	22·0	22·0
Rb	405	370	408	398	406	394	382	435	439	353	453	478	448	270	368	538	455	449	429
Sr	50	31	44	29	46	26	38	42	52	28	50	67	15	11	24	19	30	34	52
Nb	40	103	100	56	51	43	54	51	46	56	58	63	88	59	147	169	76	69	60
Mo	319	6·8	3·4	2·0	7·9	2·9	17·2	5·3	6·3	6·1	3·5	7·8	32·6	1·1	0·6	1·8	1·9	18·8	58·7
Cs	3·77	3·52	3·90	4·01	4·18	3·93	4·01	4·60	5·21	3·25	4·43	4·89	4·46	3·21	3·76	5·35	3·95	4·05	4·41
Ba	130	42	108	61	143	36	103	121	149	62	150	165	175	29	39	103	45	118	137
Ta	2·14	4·53	7·93	2·43	3·32	2·21	2·48	2·70	3·45	2·83	4·24	4·31	4·06	3·39	15·90	10·80	4·24	3·76	3·47
W	3·01	1·98	5·36	2·63	4·36	2·83	7·81	7·03	3·18	1·80	7·89	14·20	5·88	1·37	2·36	1·74	2·53	1·54	6·59
Pb	31	35	42	43	42	36	40	47	54	35	50	45	46	38	38	64	39	53	55
Th	30	18	33	30	32	19	29	33	33	26	31	30	38	18	23	23	35	29	31
U	11·8	14·4	14·9	8·8	11·6	14·0	11·3	15·6	9·0	15·6	12·2	14·3	15·7	6·1	15·4	6·3	6·7	7·6	6·3
Be	6·0	3·8	10·0	7·4	7·5	6·0	7·1	5·4	8·9	6·9	7·9	8·3	5·5	11·2	8·9	12·7	8·7	9·2	8·3
Zr	103	58·3	135	115	131	100	96·9	102	143	135	142	142	166	68·5	138	246	282	151	150
Hf	6·1	7·4	7·2	7·2	6·3	7·5	6·6	6·2	8·0	8·8	7·9	8·1	12·7	5·6	17·2	19·2	16·1	7·9	8·1
La	16·6	14·8	15·9	18·0	25·8	4·0	13·6	18·8	22·5	13·3	21·3	18·3	6·7	11·1	13·1	8·7	16·2	12·5	18·5
Ce	27·0	24·7	28·2	27·8	43·7	4·8	18·5	32·8	40·8	20·8	36·7	33·1	11·6	16·2	32·0	18·9	29·2	22·6	35·6
Pr	2·6	2·5	2·9	3·0	4·2	0·7	2·2	3·1	4·0	2·4	3·4	3·2	1·2	1·8	2·7	1·8	2·8	2·3	3·2
Nd	7·5	6·9	8·5	8·3	12·4	1·9	6·1	9·1	11·8	6·7	9·6	10·1	3·0	4·9	7·4	5·5	8·3	6·4	9·1
Sm	1·01	0·90	1·39	1·12	1·46	0·34	0·95	1·26	1·95	0·97	1·27	1·49	0·41	0·74	1·19	0·71	1·27	1·16	1·16
Eu	0·12	0·12	0·19	0·13	0·23	0·05	0·14	0·14	0·27	0·13	0·22	0·26	0·04	0·12	0·11	0·18	0·15	0·17	0·22
Gd	0·60	0·49	1·10	0·76	1·40	0·34	0·77	0·85	1·34	0·80	1·16	1·23	0·34	0·57	1·02	0·95	0·91	1·03	1·12
Tb	0·11	0·09	0·21	0·14	0·22	0·06	0·15	0·15	0·21	0·14	0·19	0·20	0·08	0·13	0·16	0·19	0·17	0·18	0·19
Dy	0·69	0·58	1·34	0·92	1·30	0·39	1·02	0·94	1·44	0·89	1·14	1·28	0·65	0·85	1·02	1·50	1·02	1·23	1·18
Ho	0·15	0·12	0·24	0·22	0·26	0·09	0·26	0·21	0·29	0·20	0·25	0·32	0·17	0·19	0·22	0·38	0·27	0·28	0·27
Er	0·57	0·45	0·96	0·84	0·99	0·39	1·00	0·76	1·08	0·73	0·87	1·17	0·75	0·72	0·88	1·71	1·04	1·05	1·02
Tm	0·11	0·09	0·22	0·17	0·23	0·08	0·20	0·15	0·24	0·15	0·19	0·26	0·18	0·14	0·20	0·44	0·26	0·24	0·21
Yb	1·01	0·95	1·94	1·58	1·81	0·86	1·80	1·33	1·97	1·40	1·83	2·50	1·83	1·32	1·81	3·77	2·44	2·23	1·92
Lu	0·20	0·18	0·37	0·33	0·37	0·20	0·37	0·27	0·43	0·26	0·36	0·54	0·41	0·27	0·39	0·78	0·55	0·43	0·43
Y	5·66	2·86	9·10	7·56	12·80	3·60	9·32	7·80	11·20	7·12	9·97	15·50	6·99	6·20	7·52	14·60	11·80	11·90	10·60
Eu*	0·47	0·55	0·47	0·43	0·49	0·45	0·50	0·41	0·50	0·45	0·56	0·60	0·33	0·56	0·31	0·67	0·42	0·46	0·59
ΣREE	58·25	52·86	63·45	63·25	94·35	14·12	47·05	69·85	88·34	48·82	78·46	74·00	27·30	39·05	62·13	45·44	64·57	51·83	74·13

Eu*, Eu anomaly.

controlled by a decease in the actual temperature alone. Therefore, we might expect rock textures to show some relationship with these trace element abundances if fluid migration is the main cause of the fractionation of fluid-mobile trace elements in the Shanggusi intrusion. However, it should be noted here that the exact components and characteristics of the fluids that contributed to the Shanggusi intrusion are difficult to address at present, owing to the limited information available. None the less, exploring the potential relationships between quantitative textural data and bulk-rock chemical variation may be helpful to investigate comprehensively what

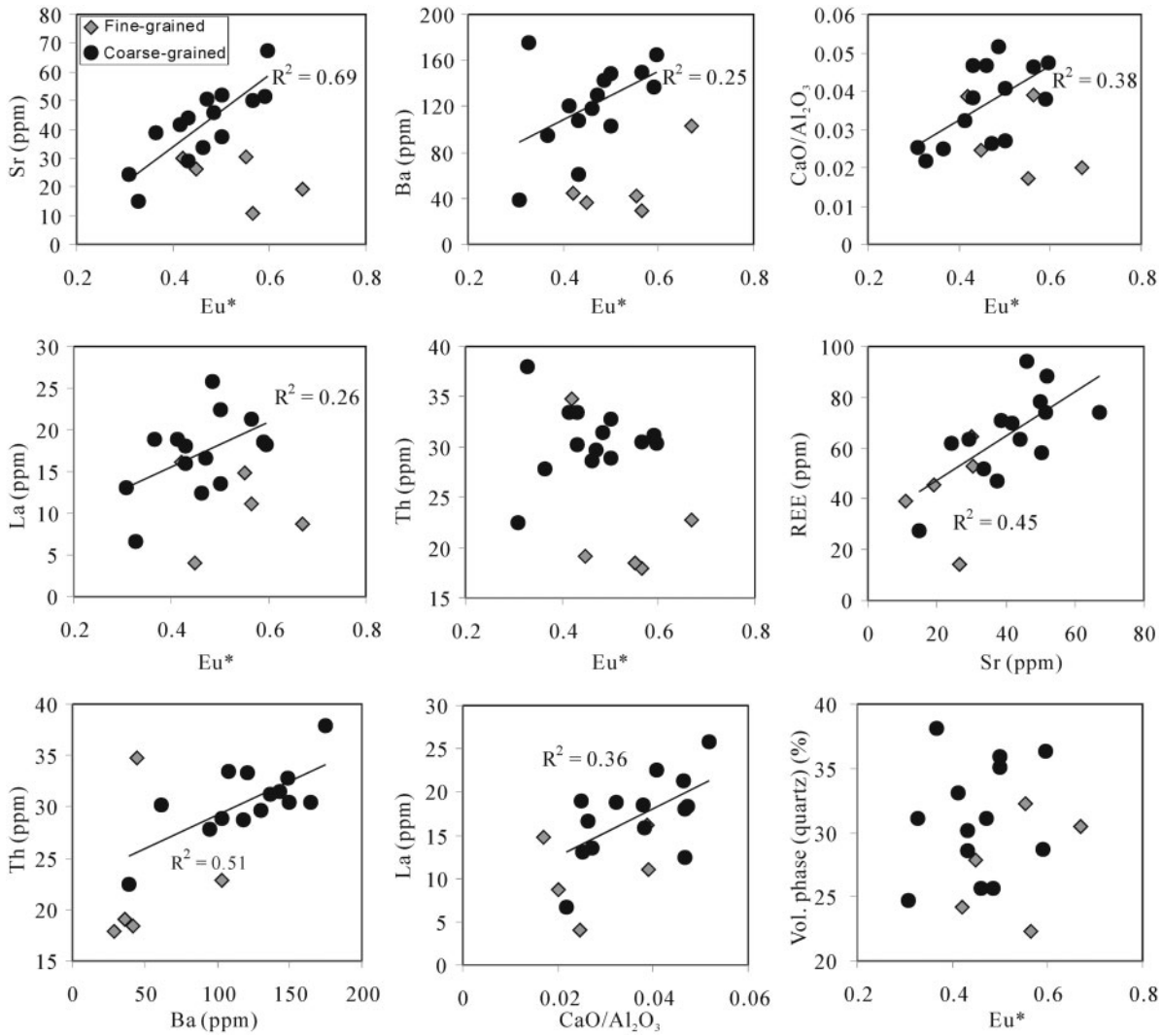

Fig. 18. Trace element co-variation diagrams for all of the samples studied. The regression lines are calculated based on the coarse-grained samples, including group 2 and samples S-7-4 and S-l2-4.

physico-chemical factors played a dominant role in the solidification of the intrusion. Such data may provide further insights into the fluid activities and chemical heterogeneities in shallow-level intrusions.

If we assume a uniform growth rate for quartz in all of the studied samples, the observed positive correlations of L_{max} with TiO_2, P_2O_5, H_2O^+, Sr, and La (Fig. 20) could result from an increase of the quartz crystallization time, reflecting accumulation of fluids that were enriched in these chemical components. It should be noted that in Fig. 20 the fine-grained samples do not show significant correlations, but they generally have relatively lower trace element contents and plot within the trends defined by the coarse-grained samples. Eu anomalies (Eu*) and ratios of CaO/Al_2O_3, La/Nb and Zr/Hf also positively correlate with L_{max}, suggesting that the fluids may affect both textural variation and the fractionation of some element ratios. Eu* shows a good negative correlation with L_{max} for the fine-grained samples. This might reflect the complex nature of the fluids, or could represent a different cooling stage, as these samples are from the granite dykes rather than the main granite porphyry. Similarly, the CSD slope of the quartz phenocrysts (including samples S-7-4 and S-l2-4) in the coarse-grained samples shows a weak positive correlation with these elements and element ratios; the fine-grained samples mostly fall within the overall trends (Fig. 2l), consistent with the suggestion that the undercooling variation is accompanied by chemical fractionation. However, the CSD slope of the groundmass from the coarse-grained samples displays a very weak correlation with trace element abundance, which might be explained by the relatively small volume melt fraction at the

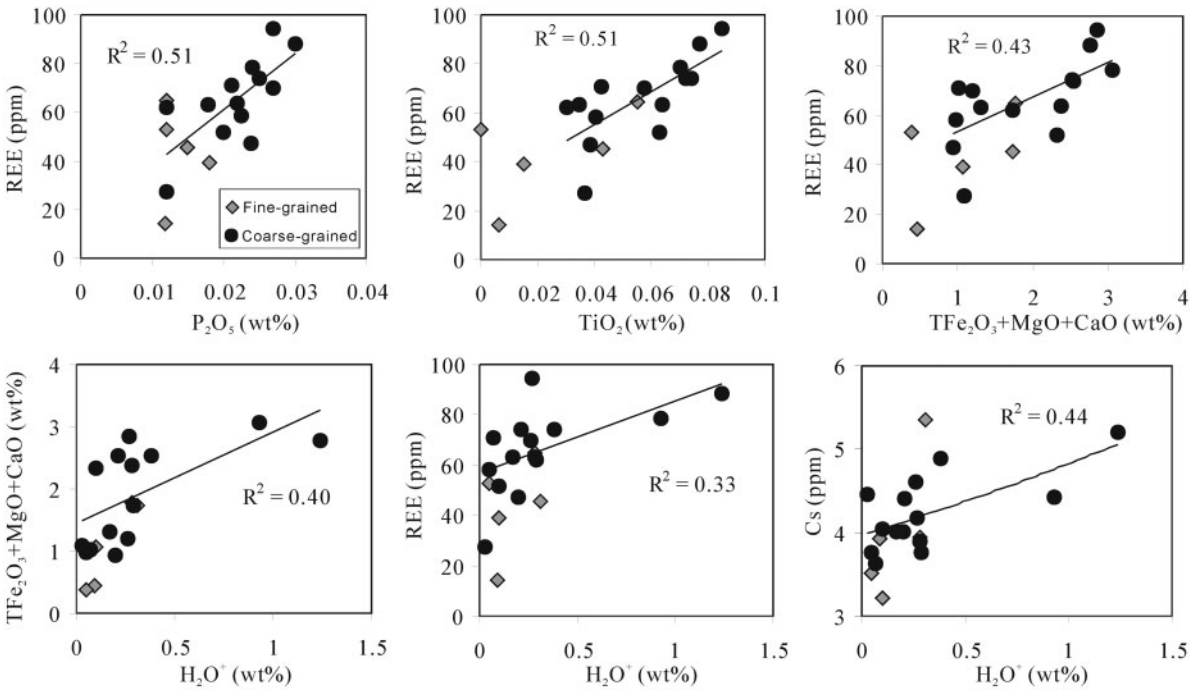

Fig. 19. Element co-variation diagrams for all of the samples studied. The regression lines are calculated based on the coarse-grained samples, including group 2 and samples S-7-4 and S-12-4.

final crystallization stage. In addition, the CSD intercept reveals similar correlations to those of the slope (not shown), indicating that, to some extent, the nucleation density is reduced by fluid-induced chemical fractionation. Hence, it can be concluded that the heterogeneity of textural and chemical characteristics is mostly controlled by the same physico-chemical factors, which are possibly the result of the migration and heterogeneous distribution of fluids.

Implications from the spatial textural variation trends

In the idealized theoretical solidification processes discussed by Zieg & Marsh (2002), when the distance from the intrusion margin is much smaller than the thickness of the intrusion, the solidus isotherms first arrive at the margins of the intrusion and gradually propagate into the center. The result of this should be that the slope and intercept vary systematically with distance from the intrusion margin. They are highest near the contact, where cooling was rapid, and lowest in the interior of the body, where cooling was slow. Figure 22a shows the spatial variations in texture in terms of CL (−1/slope) for a vertical profile through a hypothetical intrusion. The solidification process is mainly controlled by heat transfer; this has been described for large plutonic intrusions (e.g. Zieg & Marsh, 2002) and small dykes (e.g. Nkono *et al.*, 2006; Patwardhan & Marsh, 2011). In contrast to the characteristics of these hypothetical solidification processes, the slope and intercept of the groundmass are lowest on both sides of the Shanggusi granite porphyry rather than in its center. It should be noted here that the groundmass texture is a better indicator of the final solidification process after the emplacement of the intrusion, because once the intrusion has crystallized by about 50% (by volume) the intrusion no longer behaves as a magma but is now a porous crystal mush where the behaviour (motion) of the interstitial melt (or fluids) governs further crystallization; thus, it becomes rheologically improbable for the magma to convect or erupt and it becomes a rigid crystal mush (Marsh, 1981). In this context, fluids, especially hydrous fluids with low density and viscosity, if present or injected from other parts of the system, might still migrate more easily than the interstitial melt. In addition, the variation trends of the slope and intercept are not artefacts, as the photomicrographs taken of the samples from the center and both sides of the intrusion, presented in Fig. 13, display clear obvious crystal size differences. Therefore, these deviations between predicted and measured textures reveal additional processes beyond simple nucleation and growth that have contributed to the final CSD. These processes may include, for example, crystal sorting, resorption of small crystals, multiple cooling and magma injection events (Zieg & Marsh, 2002).

However, there is another, better, explanation from the perspective of undercooling that may account for the

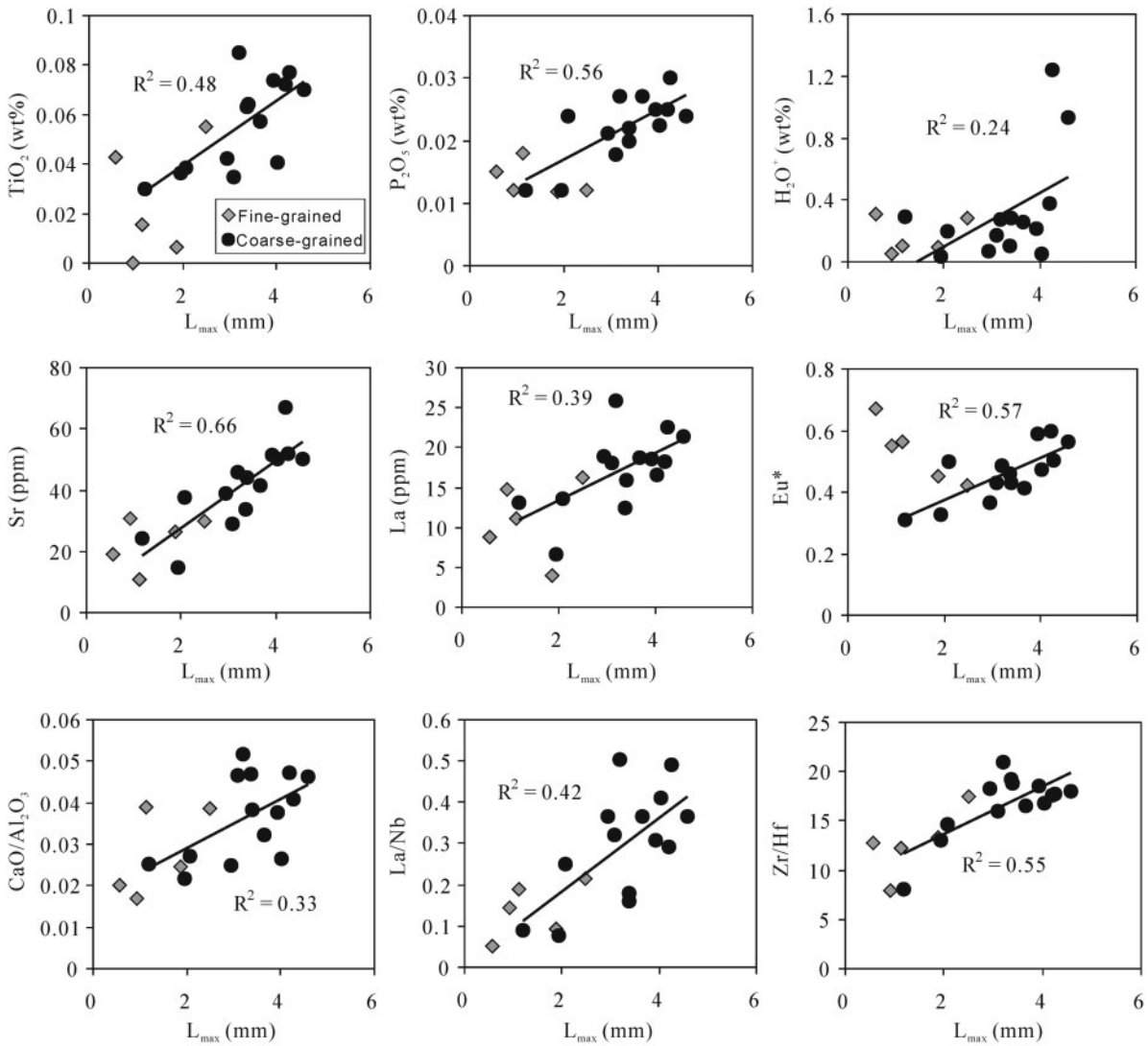

Fig. 20. Element and element ratios vs L_{max} variation diagrams for all the studied samples. The regression lines are calculated based on the coarse-grained samples, including group 2 and samples S-7-4 ($L_{max} = 2{\cdot}08$ mm) and S-12-4 ($L_{max} = 1{\cdot}19$ mm).

deviations between the predicted and measured textures. This process has been called fluid circulation and/or latent heat driven textural coarsening (e.g. Higgins, 1998, 1999, 2002*a*), where undercooling is reduced as a result of the release of latent heat and changes in the intercumulus liquid composition. Particularly coarse-grained areas may reflect focusing of circulating magmatic fluids during textural coarsening (e.g. Higgins, 2002*a*). Such an interpretation may also be partially applied here to explain the spatial textural variation of the profile of the Shanggusi granite porphyry. However, the shallower CSD slope of the groundmass on both sides of the intrusion may not be entirely produced by textural coarsening processes; it is more likely to result from a lower nucleation rate and longer crystallization time because of a reduction in undercooling. It is proposed that the migration and heterogeneous accumulation of fluids controlled the observed textural variations across the Shanggusi profile (Fig. 22b). Because fluid-bearing melts typically have lower liquidus temperatures than equivalent dry melts, the enrichment of fluids can effectively decrease the amount of undercooling and increase the solidification time. This, combined with field observations and quantitative correlations between rock textures and bulk-rock geochemistry, indicates that large amounts of fluids were probably trapped at the top of the intrusion when it was emplaced, resulting in a fluid-controlled final cooling stage rather than one controlled by isotherm regime alone. This also, to some extent, contributes to the chemical fractionation of the intrusion as discussed above. Thus, fluid

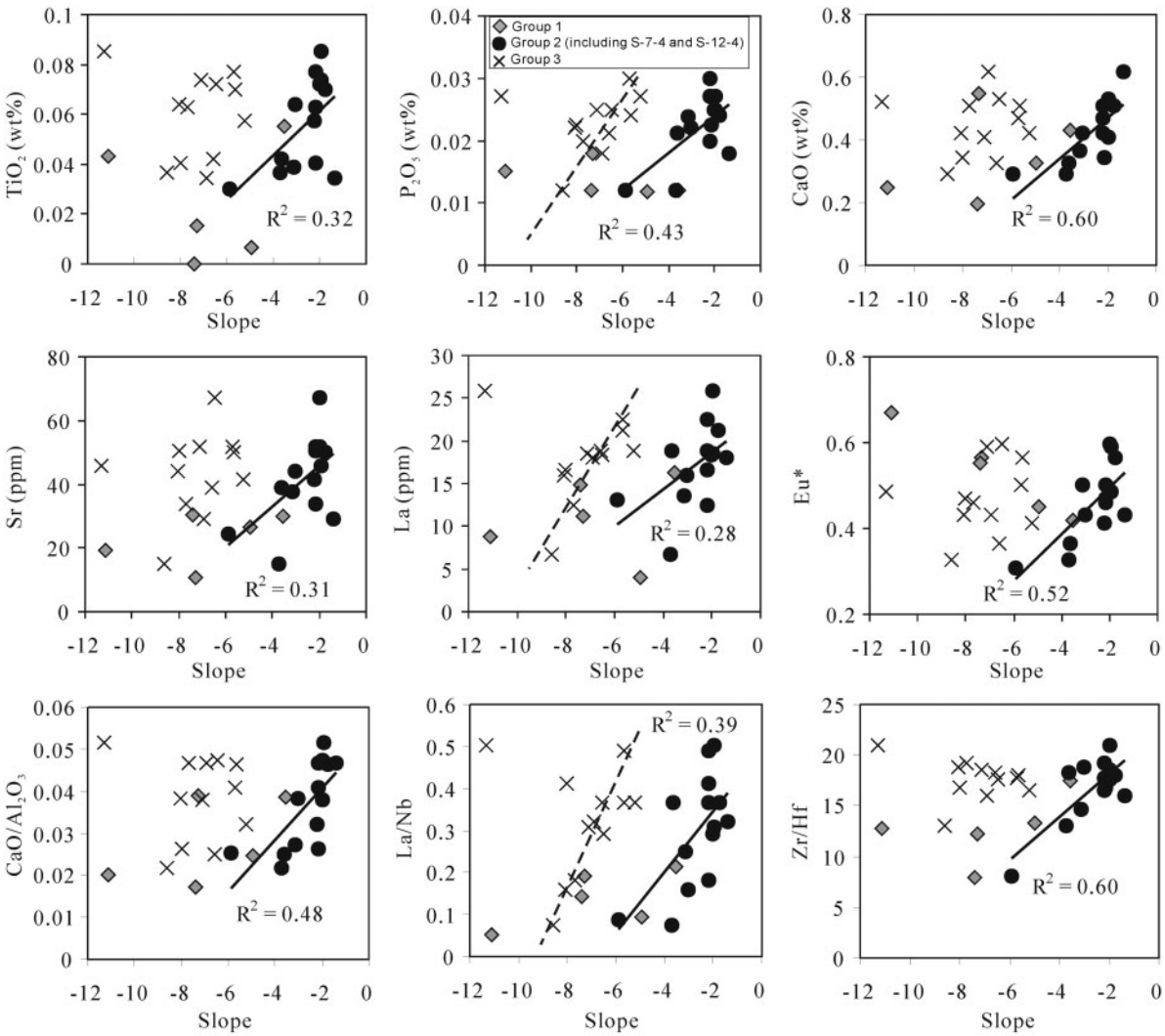

Fig. 21. Element and element ratios vs slope variation diagrams for all the studied samples. The regression lines are calculated based on the coarse-grained samples, including group 2 and samples S-7-4 and S-l2-4. Group 3 data are very scattered and the three best-fit dashed lines are drawn by ignoring the outliers.

migration-controlled undercooling, rather than the heat transfer-controlled undercooling, played a major role in the cooling history of the intrusion, and this solidification process may be a common phenomenon for shallow-level, fluid-rich granitic intrusions.

CONCLUSIONS

By integrating the geological, geochemical, mineralogical and textural data, the solidification processes for the Shanggusi granite porphyry can be summarized into three main stages as follows.

(1) The magma in the deep magma chamber partially crystallized producing quartz and feldspar phenocrysts (Fig. 23a), and the phenocryst-bearing magma was subsequently transported adiabatically to the shallow crust. Because of the sudden drop in pressure, the temperature of the water-undersaturated magma was brought closer to its liquidus temperature, resulting in the resorption of the phenocrysts of quartz and feldspar. Meanwhile, fluids, formed as the result of crystallization or injected from other parts of the system, migrated to the outer zone of the intrusion and accumulated at the top, from where they were prevented from leaking by the surrounding fine-grained pantellerite wall-rock (Fig. 23b).

(2) Because of the fluid exsolution and drop in temperature, the residual melt in the outer part of the intrusion began to crystallize rapidly. The nucleation rate suddenly changed to a new exponential rate and contributed to the typical porphyritic texture

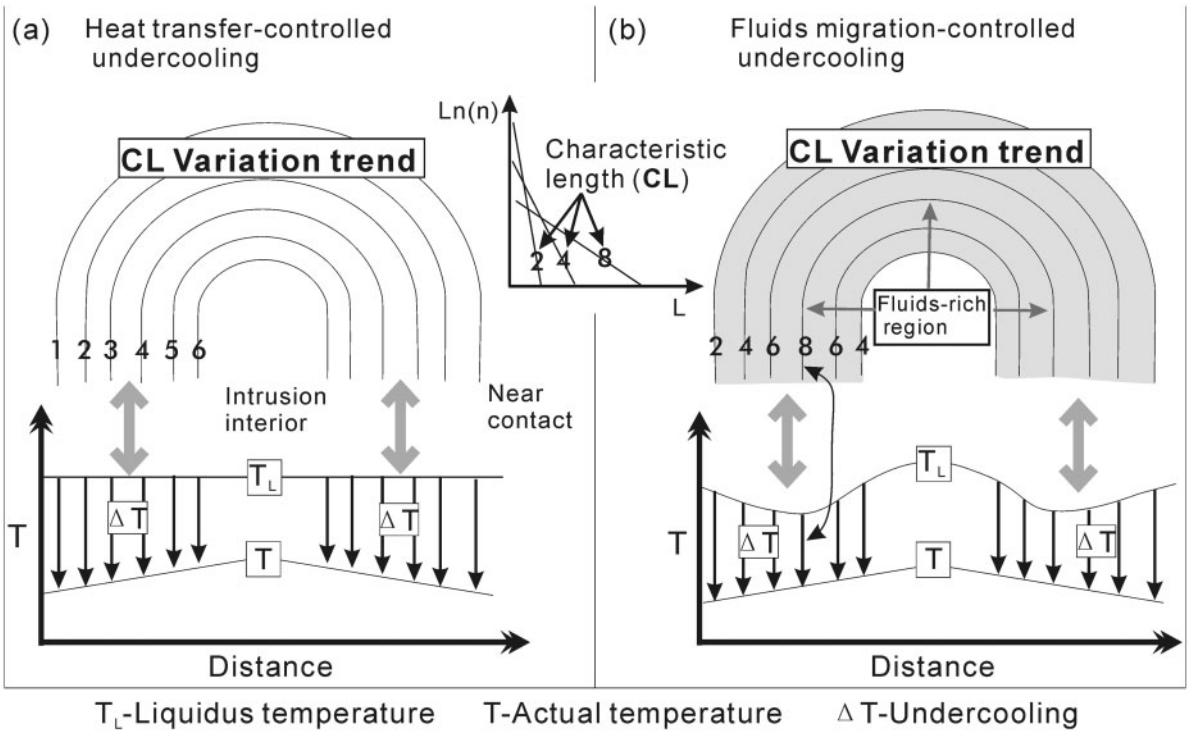

Fig. 22. (a, b) Idealized solidification processes in an intrusion showing different trends of CSD slope, intercept, and L_{max} for a single closed system. Here only CL (−1/slope) is represented. The undercooling in (a) is mainly controlled by the actual temperature (heat transfer-controlled undercooling), whereas in (b) the migration of fluids effectively changes the liquidus temperature, which mainly controls the undercooling (fluid migration-controlled undercooling). It should be noted that the lowest undercooling in (b) is produced between the margin and the center of the intrusion, and its exact location is determined by the variation trend of the liquidus temperature and isotherms. The simplified CSDs [inset between (a) and (b)] show the relationship between $\ln(n)$ and L_{max} in a single closed system; the numbers 2, 4 and 8 show the distinct characteristic length (L).

characterized by two-stage crystallization processes. However, as large amounts of fluid were concentrated at the top of the intrusion, the undercooling of the residual melt was not exclusively controlled by the temperature difference between the intrusion and its wall-rocks. It is the enrichment of fluid that decreased the degree of undercooling, resulting in an increase of the crystallization time on both sides of the intrusion that are different from those of idealized theoretical models in which the crystallization time decreases from core to margin of an intrusion.

(3) During the solidification of the outer part of the intrusion, fluid exsolution in the inner zone of the intrusion not only effectively increased the undercooling but also produced an increase in the volume, so that the magma expanded enough to fracture the overlying rocks and the outer zone of the intrusion. The residual melts in the inner zone of the intrusion were emplaced into these fractures (Fig. 23c) and solidified to form the granite dykes that are observed in the field (Fig. 23d). It should be noted that the typical phenocrysts do not exist in these granite dykes, which might be explained as follows: (a) the interior magma experienced a very low degree of undercooling that prevented its crystallization; (b) even if a small amount of crystallization occurred in the deep magma chamber, the temperature of the interior magma chamber might be closer to its liquidus temperature for long enough to dissolve almost all the phenocrysts. The granite dykes might not represent differentiated melts generated by fractional crystallization of the phenocryst-bearing magma, as both the fine- and coarse-grained samples have similar compositions and contents of rock-forming minerals, and the incompatible trace element contents of the fine-grained samples are lower than those of the coarse-grained samples. The earlier intruded granite porphyry (coarse-grained samples) and the later intruded granite dykes (fine-grained samples) possibly represent the outer part and inner part of the intrusion respectively, indicating that the incompatible element enrichment at the top of the intrusion may be the result of fluid transportation.

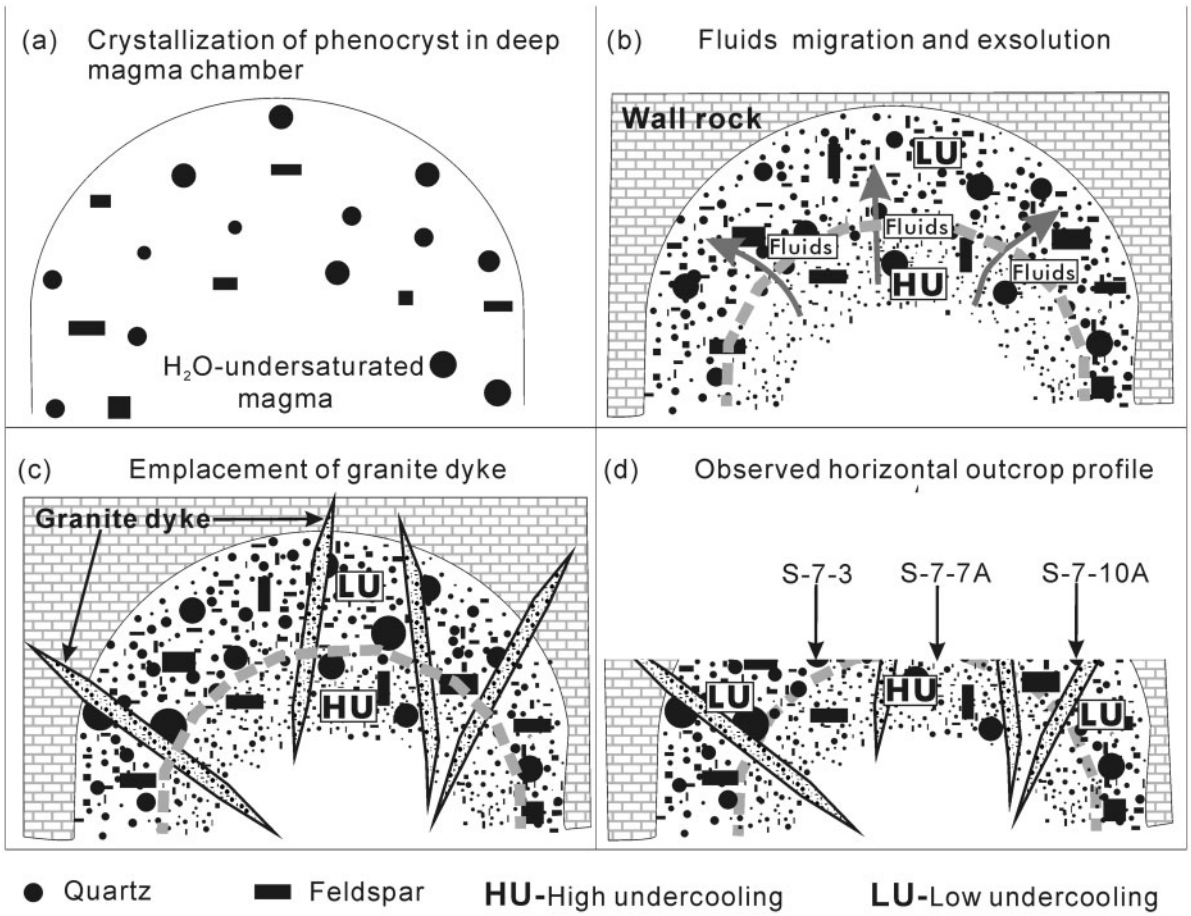

Fig. 23. Sketch of the possible solidification processes in the Shanggusi granite porphyry. (a) Quartz and feldspar (mainly alkali feldspar) crystallized in a deep magma chamber. (b) The crystal-bearing, H_2O-undersaturated magma ascends adiabatically to the shallow crust; fluids migrate to the outer zone of the intrusion and are prevented from leaking by the fine-grained pantellerite wall-rocks, giving rise to a decrease of liquidus temperature and undercooling; higher undercooling is generated in the inner zone as the result of fluid loss. (c) Fine-grained granite dykes emplaced into the solidified or crystal mush of the granite porphyry and wall-rock. (d) The observed profile. (Note the three representative samples showing different degrees of undercooling across the profile.) The dashed grey curve in (b), (c) and (d) qualitatively separates the low undercooling region from the high undercooling region.

The results of this study are consistent with an increasing number of CSD studies indicating that textural coarsening can occur during magma solidification processes and may not necessarily significantly change the bulk chemical composition of the rocks. However, the textural coarsening process may be associated with the migration of fluids, resulting in the redistribution of some fluid-mobile incompatible elements. Textural coarsening would then be accompanied by changes in the abundances of these trace elements; however, this process is much less likely to cause changes in major element compositions.

The quantitative textural characteristics of samples obtained from a horizontal outcrop profile of the Shanggusi granite porphyry reveal a solidification process associated with fluid migration-controlled undercooling, which differs from conventional models of heat transfer-controlled undercooling. If the liquidus temperature of the residual melt in an intrusion shows significant variation between the margin and the core, the fluid migration-controlled undercooling model could play a leading role; otherwise, the cooling history of an intrusion would be controlled by conductive heat transfer.

This study indicates that internal heterogeneities within apparently homogeneous magma bodies can be measured and interpreted by detailed, quantitative textural analysis, consistent with other recent CSD studies (e.g. Mock *et al.*, 2003). A model of fluid migration-controlled undercooling is proposed for the Shanggusi porphyry, based on the correlation of quantitative textural data and geochemical data. Further work is required to demonstrate if this model has more general applicability. This study suggests that quantitative correlations between textural and bulk-rock chemical characteristics can provide important physico-chemical constraints on our understanding of magma solidification processes.

ACKNOWLEDGEMENTS

I am very grateful to Zhao-Hua Luo, Xin-Xiang Lu, Bi-He Chen and Fan Huang for their help in the field. Laboratory assistance and discussions with Ying Pan, Dan-Feng Huang, Li-Lu Cheng and Jiu-Long Zhou are much appreciated. Xiang-Kun Ge is also thanked for help with the microprobe analysis. Dan J. Morgan generously provided CSDSlice and suggestions on the identification of crystal shape, and is gratefully acknowledged. Constructive and thorough reviews by Bruce D. Marsh and Michael D. Higgins, and comments from Marjorie Wilson greatly improved the quality of the paper. I finally owe many thanks to Chen-Guang Sun and Xiao-Wei Li for their comments and help with the English language.

FUNDING

This work is partially supported by the key scientific and technological projects on the geology and mineral resources of Henan Province (26417), an open research grant from the State Key Laboratory of Geological Processes and Mineral Resources, China University of Geosciences (GMPR201031) and the Fundamental Research Funds for the Central Universities (2011PY0157).

SUPPLEMENTARY DATA

Supplementary data for this paper are available at *Journal of Petrology* online.

REFERENCES

Armienti, P., Pareschi, M. T., Innocenti, F. & Pompilio, M. (1994). Effects of magma storage and ascent on the kinetics of crystal-growth—the case of the 1991–93 Mt Etna eruption. *Contributions to Mineralogy and Petrology* **115**, 402–414.

Armienti, P., Francalanci, L. & Landi, P. (2007). Textural effects of steady state behavior of the Stromboli feeding system. *Journal of Volcanology and Geothermal Research* **160**, 86–98.

Bindeman, I. N. (2003). Crystal sizes in evolving silicic magma chambers. *Geology* **31**, 367–370.

Bindeman, I. N. (2005). Fragmentation phenomena in populations of magmatic crystals. *American Mineralogist* **90**, 1801–1815.

Blundy, J. & Cashman, K. (2001). Ascent-driven crystallisation of dacite magmas at Mount St Helens, 1980–1986. *Contributions to Mineralogy and Petrology* **140**, 631–650.

Boorman, S., Boudreau, A. & Kruger, F. J. (2004). The Lower Zone–Critical Zone transition of the Bushveld Complex: A quantitative textural study. *Journal of Petrology* **45**, 1209–1235.

Borchert, M., Wilke, M., Schmidt, C., Cauzid, J. & Tucoulou, R. (2010). Partitioning of Ba, La, Yb and Y between haplogranitic melts and aqueous solutions: An experimental study. *Chemical Geology* **276**, 225–240.

Boudreau, A. E. (1995). Crystal aging and the formation of fine-scale igneous layering. *Mineralogy and Petrology* **54**, 55–69.

Boudreau, A., Mathez, E. & McCallum, I. (1986). Halogen geochemistry of the Stillwater and Bushveld Complexes: evidence for transport of the platinum-group elements by Cl-rich fluids. *Journal of Petrology* **27**, 967–986.

Cabane, H., Laporte, D. & Provost, A. (2001). Experimental investigation of the kinetics of Ostwald ripening of quartz in silicic melts. *Contributions to Mineralogy and Petrology* **142**, 361–373.

Candela, P. A. (1997). A review of shallow, ore-related granites: Textures, volatiles, and ore metals. *Journal of Petrology* **38**, 1619–1633.

Cashman, K. V. & Ferry, J. M. (1988). Crystal size distribution (CSD) in rocks and the kinetics and dynamics of crystallization III: Metamorphic crystallization. *Contributions to Mineralogy and Petrology* **99**, 401–415.

Cashman, K. & Marsh, B. (1988). Crystal size distribution (CSD) in rocks and the kinetics and dynamics of crystallization II: Makaopuhi lava lake. *Contributions to Mineralogy and Petrology* **99**, 292–305.

DeHoff, R. T. (1991). A geometrically general theory of diffusion controlled coarsening. *Acta Metallurgia et Materialia* **39**, 2349–2360.

Dulski, P. (1994). Interferences of oxide, hydroxide and chloride analyte species in the determination of rare-earth elements in geological samples by inductively-coupled plasma-mass spectrometry. *Fresenius Journal of Analytical Chemistry* **350**, 194–203.

Eberl, D. D., Kile, D. E. & Drits, V. A. (2002). On geological interpretations of crystal size distributions: Constant vs. proportionate growth. *American Mineralogist* **87**, 1235–1241.

Elliott, M. T., Cheadle, M. J. & Jerram, D. A. (1997). On the identification of textural equilibrium in rocks using dihedral angle measurements. *Geology* **25**, 355–358.

Ferlito, C. & Lanzafame, G. (2010). The role of supercritical fluids in the potassium enrichment of magmas at Mount Etna volcano (Italy). *Lithos* **119**, 642–650.

Garrido, C. J., Kelemen, P. B. & Hirth, G. (2001). Variation of cooling rate with depth in lower crust formed at an oceanic spreading ridge: Plagioclase crystal size distributions in gabbros from the Oman ophiolite. *Geochemistry, Geophysics, Geosystems* **2**, 2000GC000136.

Gualda, G. A. R. & Rivers, M. (2006). Quantitative 3D petrography using X-ray tomography: Application to Bishop Tuff pumice clasts. *Journal of Volcanology and Geothermal Research* **154**, 48–62.

Higgins, M. D. (1994). Numerical modeling of crystal shapes in thin sections: estimation of crystal habit and true size. *American Mineralogist* **79**, 113–119.

Higgins, M. D. (1996). Magma dynamics beneath Kameni volcano, Thera, Greece, as revealed by crystal size and shape measurements. *Journal of Volcanology and Geothermal Research* **70**, 37–48.

Higgins, M. D. (1998). Origin of anorthosite by textural coarsening: Quantitative measurements of a natural sequence of textural development. *Journal of Petrology* **39**, 1307–1323.

Higgins, M. D. (1999). Origin of megacrysts in granitoids by textural coarsening: a crystal size distribution (CSD) study of microcline in the Cathedral Peak Granodiorite, Sierra Nevada, California. In: Castro, A., Fernandez, C. & Vigneresse, J.-L. (eds) *Understanding Granites. Integrating New and Classical Techniques. Geological Society, London, Special Publications* **168**, 207–219.

Higgins, M. D. (2000). Measurement of crystal size distributions. *American Mineralogist* **85**, 1105–1116.

Higgins, M. D. (2002*a*). A crystal size-distribution study of the Kiglapait layered mafic intrusion, Labrador, Canada: evidence for textural coarsening. *Contributions to Mineralogy and Petrology* **144**, 314–330.

Higgins, M. D. (2002*b*). Closure in crystal size distributions (CSD), verification of CSD calculations, and the significance of CSD fans. *American Mineralogist* **87**, 171–175.

Higgins, M. D. (2006*a*). *Quantitative Textural Measurements in Igneous and Metamorphic Petrology*. Cambridge: Cambridge University Press.

Higgins, M. D. (2006*b*). Verification of ideal semi-logarithmic, lognormal or fractal crystal size distributions from 2D datasets. *Journal of Volcanology and Geothermal Research* **154**, 8–16.

Higgins, M. D. (2009). The Cascadia megathrust earthquake of 1700 may have rejuvenated an isolated basalt volcano in western Canada: Age and petrographic evidence. *Journal of Volcanology and Geothermal Research* **179**, 149–156.

Higgins, M. D. (2011). Textural coarsening in igneous rocks. *International Geology Review* **53**, 354–376.

Higgins, M. D. & Chandrasekharam, D. (2007). Nature of sub-volcanic magma chambers, Deccan Province, India: Evidence from quantitative textural analysis of plagioclase megacrysts in the giant plagioclase basalts. *Journal of Petrology* **48**, 885–900.

Higgins, M. D. & Meilleur, D. (2009). Development and emplacement of the Inyo Domes Magmatic Suite, California: Evidence from geological, textural (CSD) and geochemical observations of ash and lava. *Journal of Volcanology and Geothermal Research* **186**, 280–292.

Higgins, M. D. & Roberge, J. (2003). Crystal size distribution of plagioclase and amphibole from Soufrière Hills volcano, Montserrat: Evidence for dynamic crystallization-textural coarsening cycles. *Journal of Petrology* **44**, 1401–1411.

Higgins, M. D. & Roberge, J. (2007). Three magmatic components in the 1973 eruption of Eldfell volcano, Iceland: Evidence from plagioclase crystal size distribution (CSD) and geochemistry. *Journal of Volcanology and Geothermal Research* **161**, 247–260.

Hu, N. G., Yang, J. X., An, S. Y. & Hu, J. M. (1993). Metamorphism and tectonic evolution of the Shangdan Fault Zone, Shaanxi, China. *Journal of Metamorphic Geology* **11**, 537–548.

Inanli, F. O. & Huff, W. D. (2009). Quartz crystal size distribution of the Ordovician Millbrig K-bentonite. *Journal of Volcanology and Geothermal Research* **184**, 285–291.

Jerram, D. A., Cheadle, M. J., Hunter, R. H. & Elliott, M. T. (1996). The spatial distribution of grains and crystals in rocks. *Contributions to Mineralogy and Petrology* **125**, 60–74.

Jerram, D. A., Cheadle, M. J. & Philpotts, A. R. (2003). Quantifying the building blocks of igneous rocks: Are clustered crystal frameworks the foundation? *Journal of Petrology* **44**, 2033–2051.

Keppler, H. & Wyllie, P. J. (1990). Role of fluids in transport and fractionation of uranium and thorium in magmatic processes. *Nature* **348**, 531–533.

Lifshitz, I. M. & Slyozov, V. V. (1961). The kinetics of precipitation from supersaturated solid solutions. *Journal of Physics and Chemistry of Solids* **19**, 35–50.

Magee, C., O'Driscoll, B. & Chambers, A. D. (2010). Crystallization and textural evolution of a closed-system magma chamber: insights from a crystal size distribution study of the Lilloise layered intrusion, East Greenland. *Geological Magazine* **147**, 363–379.

Mao, J. W., Xie, G. Q., Bierlein, F., Qu, W. J., Du, A. D., Ye, H. S., Pirajno, F., Li, H. M., Guo, B. J., Li, Y. F. & Yang, Z. Q. (2008). Tectonic implications from Re–Os dating of Mesozoic molybdenum deposits in the East Qinling–Dabie orogenic belt. *Geochimica et Cosmochimica Acta* **72**, 4607–4626.

Marsh, B. D. (1981). On the crystallinity, probability of occurrence, and rheology of lava and magma. *Contributions to Mineralogy and Petrology* **78**, 85–98.

Marsh, B. D. (1988). Crystal size distribution (CSD) in rocks and the kinetics and dynamics of crystallization I. Theory. *Contributions to Mineralogy and Petrology* **99**, 277–291.

Marsh, B. D. (1998). On the interpretation of crystal size distributions in magmatic systems. *Journal of Petrology* **39**, 553–599.

Marsh, B. D. (2007). Crystallization of silicate magmas deciphered using crystal size distributions. *Journal of the American Ceramic Society* **90**, 746–757.

Mattauer, M., Matte, P., Malavieille, J., Tapponnier, P., Maluski, H., Qin, X., Lun, L. & Qin, T. (1985). Tectonics of the Qinling belt: build-up and evolution of eastern Asia. *Nature* **317**, 496–500.

Meng, Q. R. & Zhang, G. W. (1999). Timing of collision of the North and South China blocks: Controversy and reconciliation. *Geology* **27**, 123–126.

Meng, Q. R. & Zhang, G. W. (2000). Geologic framework and tectonic evolution of the Qinling orogen, central China. *Tectonophysics* **323**, 183–196.

Mills, R. D., Ratner, J. J. & Glazner, A. F. (2011). Experimental evidence for crystal coarsening and fabric development during temperature cycling. *Geology* **39**, 1139–1142.

Mock, A. & Jerram, D. A. (2005). Crystal size distributions (CSD) in three dimensions: Insights from the 3D reconstruction of a highly porphyritic rhyolite. *Journal of Petrology* **46**, 1525–1541.

Mock, A., Jerram, D. A. & Breitkreuz, C. (2003). Using quantitative textural analysis to understand the emplacement of shallow-level rhyolitic laccoliths—A case study from the Halle Volcanic Complex, Germany. *Journal of Petrology* **44**, 833–849.

Morgan, D. J. & Jerram, D. A. (2006). On estimating crystal shape for crystal size distribution analysis. *Journal of Volcanology and Geothermal Research* **154**, 1–7.

Morgan, D. J., Jerram, D. A., Chertkoff, D. G., Davidson, J. P., Pearson, D. G., Kronz, A. & Nowell, G. M. (2007). Combining CSD and isotopic microanalysis: Magma supply and mixing processes at Stromboli Volcano, Aeolian Islands, Italy. *Earth and Planetary Science Letters* **260**, 419–431.

Moss, S., Russell, J. K., Smith, B. H. S. & Brett, R. C. (2010). Olivine crystal size distributions in kimberlite. *American Mineralogist* **95**, 527–536.

Nkono, C., Femenias, O., Diot, H., Berza, T. & Demaiffe, D. (2006). Flowage differentiation in an andesitic dyke of the Motru Dyke Swarm (Southern Carpathians, Romania) inferred from AMS, CSD and geochemistry. *Journal of Volcanology and Geothermal Research* **154**, 201–221.

O'Driscoll, B., Donaldson, C. H., Troll, V. R., Jerram, D. A. & Emeleus, C. H. (2007). An origin for harrisitic and granular olivine in the Rum Layered Suite, NW Scotland: a crystal size distribution study. *Journal of Petrology* **48**, 253–270.

O'Driscoll, B., Stevenson, C. E. & Trolly, V. R. (2008). Mineral lamination development in layered gabbros of the British palaeogene igneous province: A combined anisotropy of magnetic susceptibility, quantitative textural and mineral chemistry study. *Journal of Petrology* **49**, 1187–1221.

Pamukcu, A. S., Gualda, G. A. R. & Anderson, A. T. (2012). Crystallization stages of the Bishop Tuff magma body recorded in crystal textures in pumice clasts. *Journal of Petrology* **53**, 589–609.

Pappalardo, L. & Mastrolorenzo, G. (2010). Short residence times for alkaline Vesuvius magmas in a multi-depth supply system: Evidence from geochemical and textural studies. *Earth and Planetary Science Letters* **296**, 133–143.

Patwardhan, K. & Marsh, B. D. (2011). Dynamics of the development of the Isle au Haut gabbro–diorite layered complex: quantitative implications for mafic–silicic magma interactions. *Journal of Petrology* **52**, 2365–2395.

Ratschbacher, L., Hacker, B. R., Calvert, A., Webb, L. E., Grimmer, J. C., McWilliams, M. O., Ireland, T., Dong, S. W. & Hu, J. M. (2003). Tectonics of the Qinling (Central China): tectonostratigraphy, geochronology, and deformation history. *Tectonophysics* **366**, 1–53.

Resmini, R. G. (2007). Modeling of crystal size distributions (CSDs) in sills. *Journal of Volcanology and Geothermal Research* **161**, 118–130.

Resmini, R. G. & Marsh, B. D. (1995). Steady-state volcanism, paleoeffusion rates, and magma system volume inferred from plagioclase crystal size distributions in mafic lavas—Dome Mountain, Nevada. *Journal of Volcanology and Geothermal Research* **68**, 273–296.

Rollinson, H. R. (1993). *Using Geochemical Data: Evaluation, Presentation, Interpretation*. Harlow: Longman.

Salisbury, M. J., Bohrson, W. A., Clynne, M. A., Ramos, F. C. & Hoskin, P. (2008). Multiple plagioclase crystal populations identified by crystal size distribution and *in situ* chemical data: implications for timescales of magma chamber processes associated with the 1915 eruption of Lassen Peak, CA. *Journal of Petrology* **49**, 1755–1780.

Simakin, A. G. & Bindeman, I. N. (2008). Evolution of crystal sizes in the series of dissolution and precipitation events in open magma systems. *Journal of Volcanology and Geothermal Research* **177**, 997–1010.

Stemprok, M., Dolejs, D., Muler, A. & Seltmann, R. (2008). Textural evidence of magma decompression, devolatilization and disequilibrium quenching: an example from the Western Krusne hory/Erzgebirge granite pluton. *Contributions to Mineralogy and Petrology* **155**, 93–109.

Sun, S. S. & McDonough, W. F. (1989). Chemical and isotopic systematics of oceanic basalts: implications for mantle composition and processes. In: Saunders, A. D. & Norry, M. J. (eds) *Magmatism in the Ocean Basins. Geological Society, London, Special Publications* **42**, 313–345.

Turner, S., George, R., Jerram, D. A., Carpenter, N. & Hawkesworth, C. (2003). Case studies of plagioclase growth and residence times in island arc lavas from Tonga and the Lesser Antilles, and a model to reconcile discordant age information. *Earth and Planetary Science Letters* **214**, 279–294.

Vinet, N. & Higgins, M. D. (2010). Magma solidification processes beneath Kilauea volcano, Hawaii: a quantitative textural and geochemical study of the 1969–1974 Mauna Ulu lavas. *Journal of Petrology* **51**, 1297–1332.

Wagner, C. (1961). Theorie der Alterung von Niederschlägen durch Umlosen (Ostwald-reifung). *Zeitschrift für Elektrochemie, Berichte der Bunsengesellschaft für physikalische Chemie* **65**, 581–591.

Wang, T., Wang, X. X., Zhang, G. W., Pei, X. Z. & Zhang, C. L. (2003). Remnants of a Neoproterozoic collisional orogenic belt in the core of the Phanerozoic Qinling orogenic belt (China). *Gondwana Research* **6**, 699–710.

Wang, Y. J., Fan, W. M., Peng, T. P., Zhang, H. F. & Guo, F. (2005). Nature of the Mesozoic lithospheric mantle and tectonic decoupling beneath the Dabie Orogen, Central China: Evidence from Ar-40/Ar-39 geochronology, elemental and Sr–Nd–Pb isotopic compositions of early Cretaceous mafic igneous rocks. *Chemical Geology* **220**, 165–189.

Webster, J. D. (1997). Exsolution of magmatic volatile phases from Cl-enriched mineralizing granitic magmas and implications for ore metal transport. *Geochimica et Cosmochimica Acta* **61**, 1017–1029.

Wilkinson, J., Nolan, J. & Rankin, A. (1996). Silicothermal fluid: A novel medium for mass transport in the lithosphere. *Geology* **24**, 1059.

Williams, E., Boudreau, A. E., Boorman, S. & Kruger, F. J. (2006). Textures of orthopyroxenites from the Burgersfort Bulge of the eastern Bushveld Complex, Republic of South Africa. *Contributions to Mineralogy and Petrology* **151**, 480–492.

Yang, Z. F., Luo, Z. H. & Luo, X. X. (2010). Whole rock geochemical, Nd–Pb–Sr isotopic characteristics and Re–Os ages for molybdenite of the Shangguisi granite porphyry in East Qinling. *Geochimica et Cosmochimica Acta* **74**, A1179–A1179.

Yang, Z. F., Luo, Z. H., Luo, X. X., Huang, F. & Chen, B. H. (2011). Geological characteristics and prospecting potential of the newly-discovered Shanggusi porphyry molybdenum deposit in the East Qinling. *Geology and Exploration* **47**, 1077–1090.

You, Z. D., Han, Y. J., Suo, S. T., Chen, N. S. & Zhong, Z. Q. (1993). Metamorphic history and tectonic evolution of the Qinling Complex, Eastern Qinling Mountains, China. *Journal of Metamorphic Geology* **11**, 549–560.

Zhang, G. W., Yu, Z. P., Sun, Y., Cheng, S. Y., Li, T. H., Xue, F. & Zhang, C. L. (1989). The major suture zone of the Qinling orogenic belt. *Journal of Southeast Asian Earth Sciences* **3**, 63–76.

Zhang, G. W., Dong, Y. P., Lai, S. C., Guo, A. L., Meng, Q. R., Liu, S. F., Cheng, S. Y., Yao, A. P., Zhang, Z. Q., Pei, X. Z. & Li, S. Z. (2004). Mianlue tectonic zone and Mianlue suture zone on southern margin of Qinling–Dabie orogenic belt. *Science in China Series D—Earth Sciences* **47**, 300–316.

Zieg, M. J. & Marsh, B. D. (2002). Crystal size distributions and scaling laws in the quantification of igneous textures. *Journal of Petrology* **43**, 85–101.